Aus der Klinik für Neurologie
(Prof. Dr. med. M. Bähr)
der Medizinischen Fakultät der Universität Göttingen

Cytoskeletal assembly in axonal outgrowth and regeneration analyzed using STED microscopy

INAUGURAL-DISSERTATION

zur Erlangung des Doktorgrades
der Medizinischen Fakultät der
Georg-August-Universität zu Göttingen

vorgelegt von

Max Christian Hofmann

aus

Bonn

Göttingen 2023

Dekan:	Prof. Dr. med. W. Brück

Betreuungsausschuss

Betreuer:	PD Dr. med. J. C. Koch
Ko-Betreuer:	Prof. Dr. rer. nat. T. Dresbach

Prüfungskommission

Referent/in:	PD Dr. med. J. C. Koch
Ko-Referent/in:	Prof. Dr. rer. nat. T. Dresbach
Drittreferent/in:	Prof. Dr. med. Ralf Dressel

Datum der mündlichen Prüfung:	09.01.2024

Hiermit erkläre ich, die Dissertation mit dem Titel "Cytoskeletal assembly in axonal outgrowth and regeneration analyzed using STED microscopy" eigenständig angefertigt und keine anderen als die von mir angegebenen Quellen und Hilfsmittel verwendet zu haben.

Göttingen, den ..... ……..

(Max Christian Hofmann)

Die Daten, auf denen die vorliegende Arbeit basiert, wurden teilweise publiziert:

Hofmann M, Biller L, Michel U, Bähr M, Koch JC (2022): Cytoskeletal assembly in axonal outgrowth and regeneration analyzed on the nanoscale. Sci Rep 12, 14387

Hofmann M, Biller L, Michel U, Bähr M, Koch JC (2021): Cytoskeletal assembly in axonal outgrowth and regeneration analyzed on the nanoscale. bioRxiv 2021.11.04.467310

Table of contents

List of figures ..... **III**

List of tables ..... **IV**

List of abbreviations ..... **V**

1 Introduction **1**

1.1 Axonal outgrowth and regeneration 1

1.1.1 Regeneration in the peripheral nerve system 1

1.1.2 Regeneration in the central nervous system 2

1.2 The axonal cytoskeleton 2

1.2.1 Microtubules 3

1.2.2 Actin 3

1.2.3 Spectrin 4

1.3 The membrane-associated periodic skeleton 5

1.3.1 Discovery 5

1.3.2 Structure 6

1.3.3 Properties 7

1.3.4 Development 7

1.3.5 Degeneration / Disease 7

1.3.6 Regeneration 8

1.4 Super-resolution microscopy 8

1.5 Objectives and aims 10

2 Material and Methods **11**

2.1 Materials 11

2.1.1 Chemicals and reagents 11

2.1.2 Buffers and solutions 12

2.1.3 Culture media 13

2.1.4 Machines and software 13

2.1.5 Consumables and expendables 14

2.1.6 Antibodies and staining reagents 15

2.1.7 Viral vectors 15

2.2 Methods 15

2.2.1 Viral vectors 15

2.2.2 Cell culture 16

2.2.3 Immunocytochemistry 20

2.2.4 Microscopy techniques 21

2.2.5 Analysis of microscopy data ... 22
2.2.6 Statistics ... 24

3 Results ... 25
3.1 Axonal outgrowth ... 25
3.1.1 Distribution of cytoskeletal proteins along the axon and the growth cone ... 25
3.1.2 Development of MPS ... 29
3.2 Axonal regeneration ... 34
3.2.1 Reorganization of the MPS in axonal regeneration ... 34
3.2.2 Morphological changes in axonal regeneration ... 39
3.3 Effect of calpain inhibition on regenerating axons ... 44
3.3.1 Effects on the axonal cytoskeleton ... 44
3.3.2 Effects on axonal outgrowth ... 47

4 Discussion ... 49
4.1 Introduction ... 49
4.2 Distribution of tubulin, spectrin, and F-actin along the axon and its GC ... 49
4.3 Spatial and temporal development of the MPS along the axon ... 50
4.4 Periodic patches are the building blocks of MPS formation ... 50
4.5 Role of the MPS in regulation of the axonal diameter ... 52
4.6 Spectrin periodicity is transiently increased early in axonal regeneration ... 52
4.7 Calpeptin increases spectrin periodicity ... 53
4.8 Calpain inhibition leads to enhanced axonal regeneration ... 53
4.9 Limitations ... 54
4.10 Conclusion and implications ... 54

5 Abstract ... 56

6 Appendix ... 57
6.1 Macro code: Segmenter ... 57

7 List of references ... 59

List of figures

Figure 1: Structure and cytoskeletal organization of growth cones 1
Figure 2: Representative image of a growth cone and its filopodia 4
Figure 3: Model of the MPS in axons 6
Figure 4: Principles of STED microscopy 9
Figure 5: Sequence of AAV.EGFP 16
Figure 6: Graphical explanation of axotomy procedure 20
Figure 7: Schematic depiction of a microfluidic chamber seeded with primary cortical neurons 25
Figure 8: Distribution of tubulin and spectrin along the axon 26
Figure 9: Quantified distribution of tubulin and spectrin along the axon 26
Figure 10: Localization of actin and spectrin fluorescence intensity peaks inside the GC 27
Figure 11: Relation of F-actin and spectrin in the axonal growth cone 28
Figure 12: Representative STED image of an axonal growth cone stained for F-actin and spectrin 28
Figure 13: Representative image of MPS development in an axon stained for spectrin 29
Figure 14: Development of periodicity over the length of the axon 30
Figure 15: Different stages of MPS development in different sections of the axon 31
Figure 16: Quantification of periodic patch number and length along the axon 32
Figure 17: Development of the periodic spacing of spectrin tetramers along the axon 32
Figure 18: Development of the MPS in growing axons 33
Figure 19: Increase of periodicity and reduction of axonal diameter along the axon 34
Figure 20: Representative image of axonal regeneration after an axotomy 35
Figure 21: Length of analyzed regenerating axonal segments 36
Figure 22: Comparison of MPS development of regenerating axons and non-axotomized axons 37
Figure 23: Development of axonal diameter during regeneration 38
Figure 24: Comparison of axonal outgrowth speeds of non-axotomized and regenerating axons 39
Figure 25: Representative images of GCs of regenerating axons and non-axotomized axons 40
Figure 26: Development of axonal GC area, length, and width over time 41
Figure 27: Distribution of spectrin and tubulin along regenerating axons and growth cones 42
Figure 28: Comparison of regenerating and non-axotomized axons displaying spectrin necks 43
Figure 29: Comparison of spectrin intensity distribution in axons with or without spectrin neck 43
Figure 30: Experimental procedures for treatment of axons with calpeptin or DMSO 44
Figure 31: Representative images of regenerating axons incubated with calpeptin or DMSO 45
Figure 32: Comparison of periodicity parameters between calpeptin or DMSO-treated axons 46
Figure 33: Effect of calpeptin on the number of axons displaying spectrin necks 46
Figure 34: Distribution of spectrin in axons treated with DMSO or calpeptin 47
Figure 35: Effects of calpeptin on axonal outgrowth and regeneration 48

List of tables

Table 1: Chemicals and reagents 11
Table 2: Buffers and solutions 12
Table 3: Used culture media and media production 13
Table 4: Machines and software 13
Table 5: Consumables and expendables 14
Table 6: Antibodies and staining reagents 15

List of abbreviations

AAV	Adeno-associated viral vector
ANOVA	Analysis of variance
BDNF	Brain-derived neurotrophic factor
BSA	Bovine serum albumin
CCD	Charge-coupled device
CM	Cortex cell culture media
CM+	Cortex cell culture media with FCS
CM++	Cortex cell culture media with FCS and growth factors
CM0+	Cortex cell culture media without FCS, but with growth factors
CMF	Calcium- and magnesium-free media
CNS	Central nervous system
CNTF	Ciliary neurotrophic factor
DIV	Day *in vitro*
DMSO	Dimethyl sulfoxide
DNAse	Deoxyribonuclease I
EGFP	Enhanced green fluorescent protein
EGTA	Ethylene glycol-bis(2-aminoethylether)-N,N,N',N'-tetraacetic acid
F-actin	Filamentous actin
FBS	Fetal bovine serum
GC	Growth cone, structure at the tip of an extending axon
HBSS	Hank's balanced salt solution
HEPES	2-[4-(2-Hydroxyethyl)piperazin-1-yl]ethanesulfonic acid
IC	Incubation chamber
LED	Light-emitting diode
MFC	Microfluidic chamber
$MgCl_2$	Magnesium chloride
MPS	Membrane-associated periodic skeleton
MSR	Multi-sensor rack file format
NMII	Non-muscle myosin II
PBS	Phosphate-buffered saline
PDMS	Polydimethylsiloxane
PFA	Paraformaldehyde
PHEM	PIPES, HEPES, EGTA, MgCl2
PIPES	1,4-Piperazinediethanesulfonic acid
PLO	Poly-L-ornithine
PNS	Peripheral nervous system
PSN	Penicillin-streptomycin-neomycin antibiotic mixture

RPM	Rounds per minute
spectrin	βII-Spectrin
STED	Stimulated emission depletion
STORM	Stochastic optical reconstruction microscopy
TIFF	Tagged image file format
TRIS	Tris(hydroxymethyl)aminomethane
TU	Transduction units
tubulin	βIII-Tubulin
UK	United Kingdom
USA	United States of America

1 Introduction

1.1 Axonal outgrowth and regeneration

Since the first description of growing axons by Ramon y Cajal (1890) at the end of the 19th century, researchers have been fascinated by the ability of neurons to cover very long distances with their axons. In humans, axons can cover very long distances of up to one meter while maintaining a very thin diameter of 0.1 – 10 μm (Graf von Keyserlingk and Schramm 1984; Greenberg et al. 1990).

Axons need to reliably reach their target during axonal outgrowth by following molecular cues like growth factors (Tessier-Lavigne and Goodman 1996). This cue-finding is mediated by the tip of the axon, the growth cone (GC; **Figure 1**). This highly motile structure moves by protrusion and retrusion of filopodia and retrograde flow of actin (Lowery and Van Vactor 2009). Additionally, the coupling of the cytoskeleton to the substrate enables both axon and GC to generate pulling and traction forces (Heidemann et al. 1990).

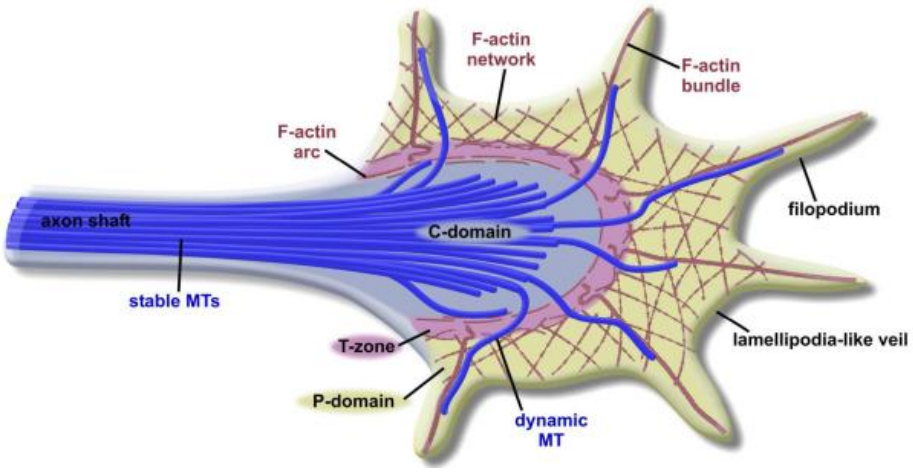

Figure 1: Structure and cytoskeletal organization of growth cones. The GC sits on top of the growing axon and facilitates outgrowth and cue-finding. The GC can be divided into three zones: the central zone (or C-domain), the transition zone (or T-zone), and the peripheral zone (or P-domain). From the axonal shaft (to the left), microtubules extend into the central zone. A filamentous actin (F-actin) arc defines the transition zone. The GC extends its lamellipodium and filopodia from the peripheral zone, mainly supported by F-actin (Lowery and Van Vactor 2009). The figure was used with the kind permission of [Springer Nature; license number: 5140140138957].

1.1.1 Regeneration in the peripheral nerve system

In the human peripheral nervous system (PNS), axons can regenerate after trauma. While the distal portion degenerates in a process called Wallerian degeneration, the proximal portion readily regenerates (Huebner and Strittmatter 2009).

A successful regeneration depends on multiple steps (Bradke et al. 2012). As the integrity of the axonal membrane is compromised, extra-cellular calcium flows into the axon. This calcium elevation inside the axon triggers the sealing of the dissected axonal membrane (Fishman and Bittner 2003) and the reformation of the axonal cytoskeleton to form a new growth cone (Sahly et al. 2006). This reformation begins with the cleavage of cytoskeletal proteins and structures like actin, spectrin, and microtubules. After the membrane is sealed with an accumulation of vesicles and the intra-axonal calcium levels are normalized, actin and microtubules repolymerize to form the new GC.

This ability of PNS-axons to regenerate can be utilized in therapeutic approaches like direct suturing of dissected nerves, nerve autografts, and decellularized nerve graft transplantation (Houschyar et al. 2016). However, the ability to regenerate can also lead to unwanted pathologies, like Frey's syndrome, where regenerating parasympathetic axonal sprouts stimulate the scalp's sweat glands instead of parotid salivary glands (Gardner and McCubbin 1956).

1.1.2 Regeneration in the central nervous system

In the adult central nervous system (CNS), however, axons generally fail to regenerate after trauma (Tedeschi and Bradke 2017). In experimental setups, CNS-axons seem to be capable of regeneration to some extent, but newly formed growth cones do not survive longer time periods and are not capable of extending over longer distances (Liu and Chambers 1958; Taylor et al. 2006; Fitch and Silver 2008). This problem is an ongoing topic for scientific and clinical research. Experimental models have shown that the molecular structure of glial scars, which form after trauma, as well as the release of inhibitory compounds by astrocytes, are important variables in regenerative failure (Pasterkamp et al. 2001; Apostolova et al. 2006). But also the cytoskeleton has a major role in successful regeneration and outgrowth in the CNS, as the stabilization of microtubules allows dissected axons to cross inhibitory glial scars (Sengottuvel et al. 2011)

1.2 The axonal cytoskeleton

The axonal cytoskeleton plays a crucial role in facilitating axonal outgrowth. It is composed of three main components: neurofilaments, microtubules, and actin filaments (Leterrier et al. 2017). Neurofilaments mainly control the axonal diameter, and therefore the electrical conductivity (Friede and Samorajski 1970). Microtubules and actin are highly dynamic structures that facilitate axonal outgrowth and transport of axonal cargo (Kevenaar and Hoogenraad 2015).

1.2.1 Microtubules

Microtubules are polymers of α- and β-tubulin molecules (Weisenberg 1972) that form long and dynamic structures (Mitchison and Kirschner 1984) with a diameter of 23 – 27 nm (Ledbetter and Porter 1963). Microtubules generally have a rapidly growing plus end (Mitchison 1993) and a slower growing minus end (Cote and Borisy 1981). Microtubules are essential for cellular stabilization and axonal transport (Morris and Hollenbeck 1995).

While many tubulin molecules are expressed throughout different cell types, neurons express a specific form of β-tubulin, named βIII-tubulin (Caccamo et al. 1989). This neuron-specific expression allows to differentiate neurons from glial cells in cell cultures by immunocytochemistry because glial cells lack βIII-tubulin.

In axonal outgrowth, microtubules play an important role. Microtubule plus ends are directed towards the distal axon (Baas et al. 1988). As the axon extends, microtubules splay into the GC and consolidate this region as the newly formed axon (Buck and Zheng 2002). Microtubules are also, to some extent, involved in GC steering (Buck and Zheng 2002). Important for the initial outgrowth of neurites is also the sliding of microtubules along other microtubules, mediated by kinesin-1 (Lu et al. 2013).

1.2.2 Actin

Actin is a globular protein (G-actin) that is present in almost all eukaryotic cells. G-actin can assemble into longer filaments, filamentous actin (F-actin), supporting cell motility, cell stability, and muscle contraction in muscle cells (Parker et al. 2020). Furthermore, actin enables cell polarity (Kapitein and Hoogenraad 2011), intracellular transport of cargoes (Pollard and Cooper 2009), and axonal outgrowth (Dent and Gertler 2003). F-actin is accompanied by a multitude of proteins that stabilize or destabilize the filament or integrate F-actin into the cytoskeleton.

Figure 2: Representative image of a growth cone and its filopodia. Stimulated emission depletion microscopy image of an axon and its growth cone displaying an F-actin stain (red), merged with a confocal image of the same section, showing transduced enhanced green fluorescent protein (EGFP; green). F-actin filaments extend from the growth cone. Rat cortical neurons were cultured in microfluidic chambers (MFC) and fixed on day *in vitro* (DIV) 11. The scale bar is 5 µm.

As can be seen in **Figure 2**, F-actin drastically shapes the axonal GC and its filopodia. The respective processes of protrusion and retrograde flow of actin in the GC, combined with the stabilizing outgrowth and kinesin-1 mediated sliding of microtubules along the axon, allow the axon to elongate (Flynn et al. 2012; Lu et al. 2013). The protrusion and retrograde flow of F-actin, also termed actin treadmilling, facilitates the GCs' highly dynamic movement. During actin treadmilling, filaments assemble at the extremities of the lamellipodium and filopodia and disassemble in the transition zone inside the growth cone, creating a backward flow (Schaefer et al. 2002). This backward flow is then coupled to the substrate, creating traction, force, and movement (Heidemann et al. 1990).

1.2.3 Spectrin

Spectrin is a heterodimeric cytoskeletal protein first isolated from erythrocytes (Marchesi and Steers 1968). The heterodimer is made up of an α- and a β-subunit, connected through hydrophobic bonds (Grum et al. 1999). Two heterodimers, connected head by head, form a spectrin tetramer with a length of 200 nm (Brown et al. 2015). In erythrocytes, these spectrin tetramers are generally made up of two αI-spectrin and two βI-spectrin subunits. Close to

the membrane of erythrocytes, spectrin tetramers form hexagonal arrangements of six spectrin tetramers connected to a short actin filament, capped by adducin (Fowler 2013). The sub-membranous arrangement of spectrin provides flexibility and allows for the deformation of erythrocytes passing through small blood vessels (Lux IV 2016).

Using live imaging, spectrin was soon discovered in axons as an unknown protein being transported along axons, originally named fodrin (Levine and Willard 1981). The α-subunit of neuronal spectrins is always made up of αII-spectrin and the β-subunit of either βI, βII, βIII, βIV, or βV-spectrin (Liu and Rasband 2019). While βII-spectrin is widely distributed in neurons and their axons (Xu et al. 2013), βIII-spectrin is found in dendrites and the soma of neurons (Han et al. 2017), and βIV-spectrin is found explicitly at the axon initial segment and in the nodes of Ranvier (Berghs et al. 2000).

Recently, there has been an increasing interest in βII-spectrin due to its diverse and essential roles in axons. βII-spectrin is encoded by the *SPTBN1*-gene and is the most common non-erythroid spectrin. Different studies estimate the length of βII-spectrin tetramers to be around 150 – 250 nm (Bennett et al. 1982; Xu et al. 2013).

Expression of βII-spectrin is critical for the survival of embryos (Lorenzo et al. 2019), and deletion of β-spectrin leads to breakage of axons in worms (Hammarlund et al. 2007). βII-spectrin also is an important protein for linking vesicles to microtubule motor proteins, allowing axonal transport (Holleran et al. 1996; Takeda et al. 2000).

1.3 The membrane-associated periodic skeleton

1.3.1 Discovery

Recent advances in super-resolution microscopy set the path for the discovery and characterization of biological structures on a nanoscale level. The most remarkable discovery was a periodic, lattice-like arrangement of spectrin, actin, and adducin close to the membrane of axons, the membrane-associated periodic skeleton (MPS) (Costa and Sousa 2021). The MPS was described first by Xu et al. (2013) using stochastic optical reconstruction microscopy (STORM). In the competing race of the emerging super-resolution microscopy techniques, the existence of the MPS was soon confirmed using stimulated emission depletion (STED) microscopy (Lukinavičius et al. 2014).

Initially discovered in fixed, cultured hippocampal neurons and brain slides (Xu et al. 2013), the MPS was also confirmed in living neurons (Lukinavičius et al. 2014; D'Este et al. 2015), as well as in most other types of neurons and animal species *in vitro* (D'Este et al. 2016; He et al. 2016). Divergent from the first assumption that the MPS was axon specific, it was also discovered in dendrites (Zhong et al. 2014), dendritic spines (Bär et al. 2016), and the neuronal cell body (Han et al. 2017; Hauser et al. 2018). The broad distribution of MPS

throughout the nervous system points to an essential role in neuronal function (Costa and Sousa 2021).

1.3.2 Structure

Inherent to the structure of the MPS lies the reason for its relatively late discovery: the periodic spacing of actin molecules (see **Figure 3**) at a distance of around 190 nm, which lies below Abbes diffraction limit of around 200 nm (Abbe 1873).

The MPS was first described as a periodic arrangement of actin rings, interconnected by spectrin tetramers, at a spacing of 180 – 190 nm between two actin rings (Xu et al. 2013). Adducin and ankyrin-B were also identified as part of the MPS, the latter in a semi-periodic fashion due to its different binding patterns. It was suggested initially that actin rings are made up of short actin filaments, capped and stabilized by adducin (Leite et al. 2016). A more recent study identifies the actin rings as long, braided actin filaments, using combined single-molecule localization microscopy and platinum-replica electron microscopy (Vassilopoulos et al. 2019). In the latter model, adducin would therefore enhance the lateral binding of actin and spectrin. The exact form of actin in the MPS has yet to be determined conclusively.

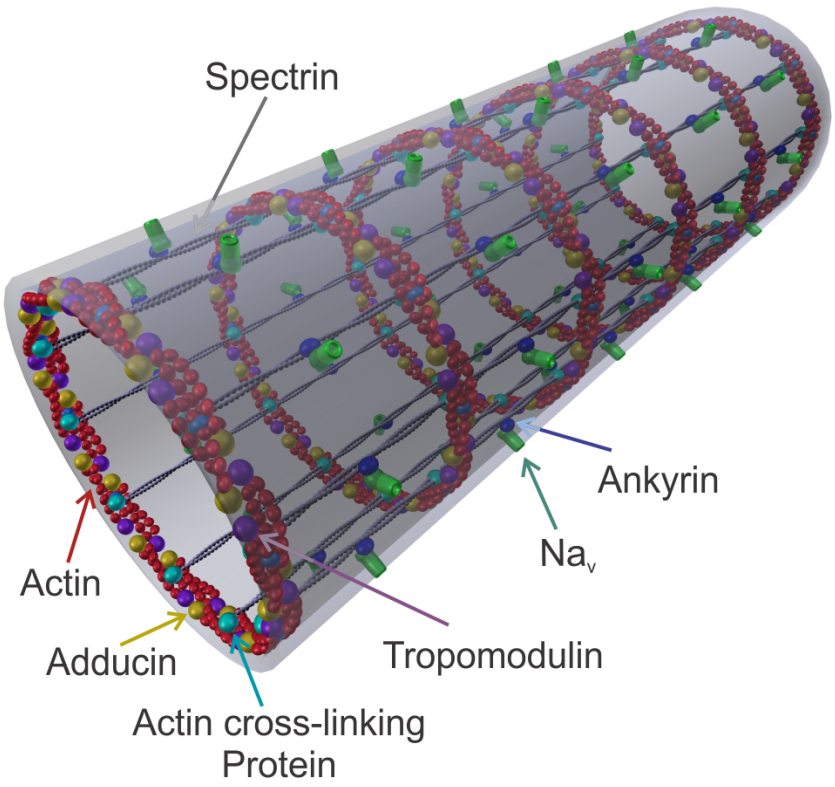

Figure 3: Model of the MPS in axons. Graphical model of the periodic arrangement of actin, spectrin, and accompanying proteins, based on SRM (Xu et al. 2013). Circumferential actin rings (red) are interconnected by spectrin tetramers. Ankyrin links spectrin to the axonal cell membrane. Adducin may cap actin filaments or enhance lateral binding to spectrin tetramers. Different proteins are periodically distributed along the MPS, for example, ion channels (figure adapted and modified from Zhang et al. 2017; Copyright: CC BY 4.0).

Another molecule found in the structure of the MPS is non-muscle myosin II (NMII), which is known to have a role in regulating axonal diameter (Fan et al. 2017). Platinum-replica electron microscopy recently also suggested that NMII molecules crosslink adjacent actin rings, providing increased stability and contractility (Vassilopoulos et al. 2019). Thus, the linking of individual actin rings by NMII could create the force needed for influencing axonal diameter (Costa et al. 2020; Zhou et al. 2022).

1.3.3 Properties

The MPS is involved in a multitude of cellular functions. This includes mechanical properties, like stabilization of axons (Hammarlund et al. 2007; Dubey et al. 2020), involvement in electrical conductivity (Costa et al. 2020), the control of axonal diameter (Leite et al. 2016; Costa et al. 2020; Wang et al. 2020), axonal transport of cargoes (Wang et al. 2020), and the lattice-like organization of proteins into the axon (Xu et al. 2013; Vassilopoulos et al. 2019; Zhou et al. 2019; Li et al. 2020).

1.3.4 Development

The development and formation of the MPS is an ongoing topic. Studies have suggested a development of the MPS in a proximal to distal pattern (Zhong et al. 2014; Han et al. 2017; Lorenzo et al. 2019). The formation of the MPS is thought to start close to the soma at an early stage of axonal development and then progresses towards the more distal parts of the axon over time. *In vitro,* spectrin tetramers form a periodic arrangement at DIV 2 (Zhong et al. 2014), whereas actin rings were detected from DIV 5 – 7 (Xu et al. 2013). *In vivo*, periodic actin rings and periodic spectrin tetramers are assembled simultaneously already at DIV 2 (D'Este et al. 2015). This inconsistency may be due to the decreased ability of fixed immature neurons to withstand the permeabilization process necessary for the staining of F-actin using phalloidin (Leite and Sousa 2016). The actin-binding molecule adducin is incorporated into the MPS at DIV 8 (Zhong et al. 2014). In vitro, the experimental knockout of adducin lead to increased axonal diameter, but axons lacking adducin still decreased in diameter during culture, suggesting other molecules are also involved in regulating axonal diameter (Leite et al. 2016). The proximal to distal development and the decrease in axonal diameter during culture suggest a constricting function of the MPS (Leite et al. 2016). In the soma of neuronal stem cells, short periodic patches showing a 1D arrangement of actin and spectrin were discovered (Hauser et al. 2018). Once matured, these neurons then displayed a mature MPS. The exact sequence of this development remains unknown.

1.3.5 Degeneration / Disease

Previous publications have discussed the role of the MPS in axonal degeneration (Unsain et al. 2018; Wang et al. 2019). The stabilization of F-actin using the drug cucurbitacin-B reduced axonal degeneration and stabilized the MPS (Unsain et al. 2018). Trophic factor withdrawal

led to a rapid disruption of the MPS during axonal degeneration, but this loss was independent of caspase apoptotic pathways (Wang et al. 2019).

βII-Spectrin knockout mice lack long axonal bundles connecting cerebral hemispheres, show motor deficits, and die at an early postnatal stage (Galiano et al. 2012; Lorenzo et al. 2019). Mutations in the gene coding for αII-spectrin in humans can lead to early infantile epileptic encephalopathies with progressive brain atrophy (Lorenzo 2020). Likewise, mutations in *SPTBN2* can cause spinocerebellar ataxia type 5 in humans (Ikeda et al. 2006). This gene codes for βIII-spectrin, which can be found periodically distributed in the soma and neurites of neurons (Han et al. 2017).

1.3.6 Regeneration

So far, the role of the MPS in axonal regenerating has not been explored. The rapid disruption of the MPS in degenerating axons raises the question of whether axons need to reassemble their MPS in order to facilitate regeneration. Is the MPS crucial for regeneration? Or would a stabilization of the MPS in leasoned axons hinder regeneration? In a review, Leite and Sousa (2016) hypothesized that regenerating axons might assemble their MPS more efficiently.

So far, stabilization of the MPS using actin-stabilizing drugs has been tested (Unsain et al. 2018; Wang et al. 2019), but not by stabilization of spectrin. Indirect stabilization of spectrin could be achieved by inhibition of the enzyme Calpain. Calpain is a spectrin cleavage enzyme that is activated shortly after axotomy by an influx of calcium, causing spectrin structures to be destroyed (Zhang et al. 2016). Calpain can be inhibited using the drug calpeptin.

1.4 Super-resolution microscopy

For almost 150 years, the limit of (light) microscopical resolution was believed to be around 200 nm, as it was postulated by Ernst Abbe (1873). Abbe discovered that spatial resolution is limited by the wavelength of light and the aperture of the used optics. In recent years, the field of super-resolution microscopy has emerged at the borderlines between biology, chemistry, and physics. New microscopy techniques allowed for the discovery of biological structures that were previously hidden due to the diffraction limit.

One of these techniques is STED microscopy. First described by Hell and Wichmann (1994) and rewarded with a Nobel prize, STED microscopy allows for a maximum resolution down to around 20 nm.

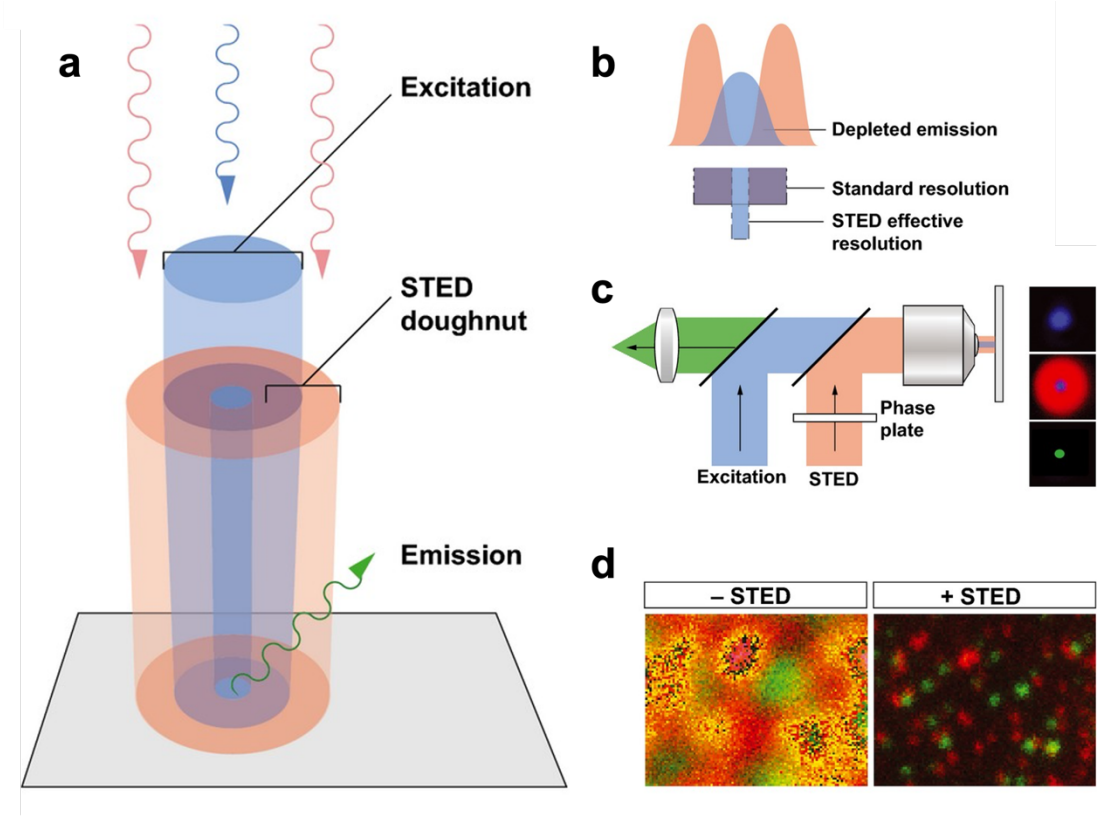

Figure 4: Principles of STED microscopy. (a) shows a 3D-illustration of the spatial placement of the excitation beam and the STED depletion doughnut beam. A laser is used to excite (blue) a probe with a doughnut-shaped depletion beam aligned over the excitation laser beam. Fluorescence emission is, therefore, emitted only from the non-depleted beam at the hole of the doughnut. **(b)** shows the improvement of effective resolution achieved by the use of the depletion beam to minimize the area of emission. In **(c)**, the standard setup of a STED microscope is depicted in a schematic diagram. A phase plate shapes the STED beam into a doughnut-shaped form, the beam is then aligned with the excitation beam, resulting in a minimized area of emission (green point). Examples of fluorescent beads (red and green) imaged using STED and conventional fluorescence microscopy are shown in **(d)**. STED microscopy allows for signal discrimination at a nanoscale level. Figure adapted from (Blom and Brismar 2014), used with the kind permission of [John Wiley and Sons; license number: 5393731082471].

Based on the principles of confocal laser-scanning microscopy, a doughnut-shaped depletion laser is added to the microscope setup (see **Figure 4)**. This depletion laser beam is aligned with the excitation laser and depletes all emission except the intensity nadir at the doughnut hole. This results in a significantly reduced emission area and, finally, a much higher resolution.

1.5 Objectives and aims

Axonal outgrowth and regeneration are closely linked to the axonal cytoskeleton. It must tolerate mechanical stress and torsion while also allowing for adaptation and response to trauma or injury, such as axonal lesions. The cytoskeletal proteins actin, spectrin, and adducin form highly periodic structures in the axon, known as the membrane-associated periodic skeleton, discovered through recent breakthroughs in super-resolution imaging. A wide variety of studies have been conducted to investigate the role of the MPS and its involvement in axonal processes. It was suggested that the MPS develops in a proximal to distal manner along the axon. Despite recent interest in the MPS and its development, the precise sequence of MPS formation and development in physiologically outgrowing axons is still unknown. The assembly and role of the MPS in regenerating axons are unclear as well. Therefore, the aim of the present study was to characterize the development of the MPS in growing axons and the cytoskeletal changes upon regeneration after axotomy. A further goal was to analyze the effect of inhibiting the spectrin-cleaving enzyme calpain using the drug calpeptin on the MPS. Therefore, a microfluidic approach was used to cultivate embryonic cortical neurons of the rat and to accomplish axonal isolation. To analyze the MPS of physiologically outgrowing and regenerating axons, axons were assessed using STED microscopy.

2 Material and Methods

2.1 Materials

2.1.1 Chemicals and reagents

Table 1: Chemicals and reagents

Chemicals and reagents	**Manufacturer**
Ammonium chloride	AppliChem, Darmstadt, Germany
B27 Supplement	Gibco, Waltham, MA, USA
BDNF (Brain-derived neurotrophic factor)	Pepro Tech, Rocky Hill, NJ, USA
BSA (Bovine Serum Albumin)	Jackson Immuno Research, West Grove, PA, USA
Calpeptin	Sigma Aldrich, St. Louis, MO, USA
CNTF (Ciliary neurotrophic factor)	Pepro Tech, Rocky Hill, NJ, USA
DMSO (Dimethyl sulfoxide)	AppliChem, Darmstadt, Germany
DNAse I (Deoxyribonuclease)	Roche, Basel, Swiss
EGTA (Ethylene glycol-bis(2-aminoethyl-ether)-*N*,*N*,*N*′,*N*′-tetraacetic acid)	AppliChem, Darmstadt, Germany
Ethanol	AppliChem, Darmstadt, Germany
FBS (Fetal bovine serum) Superior	Biochrom, Berlin, Germany
Glutaraldehyde	AppliChem, Darmstadt, Germany
Glycin	AppliChem, Darmstadt, Germany
HBSS (Hank's balanced salt solution)	Gibco, Waltham, MA, USA
HEPES (2-[4-(2-Hydroxyethyl)piperazin-1-yl]ethanesulfonic acid)	AppliChem, Darmstadt, Germany
Holo-Transferrin	AppliChem, Darmstadt, Germany
L-Glutamax	Gibco, Waltham, MA, USA
Laminin	Sigma Aldrich, St. Louis, MO, USA
Methanol	AppliChem, Darmstadt, Germany
$MgCl_2$ (Magnesium chloride)	AppliChem, Darmstadt, Germany
Neurobasal Medium (1x)	Gibco, Waltham, MA, USA
PBS (Phosphate-buffered saline solution)	AppliChem, Darmstadt, Germany
PFA (Paraformaldehyde)	AppliChem, Darmstadt, Germany
PIPES (1,4-Piperazinediethanesulfonic acid)	AppliChem, Darmstadt, Germany
PLO (Poly-L-ornithine)	Sigma Aldrich, St. Louis, MO, USA
Ponceau S	Sigma Aldrich, St. Louis, MO, USA

Chemicals and reagents	**Manufacturer**
PSN (Penicillin-streptomycin-neomycin antibiotic mixture)	Gibco, Waltham, MA, USA
Sodium bicarbonate 7.5%	Gibco, Waltham, MA, USA
TRIS (Tris(hydroxymethyl)aminomethane)	AppliChem, Darmstadt, Germany
TritonX-100	AppliChem, Darmstadt, Germany
Trypsin	Sigma Aldrich, St. Louis, MO, USA

2.1.2 Buffers and solutions

Table 2: Buffers and solutions

Buffers and solutions	**Production**
BDNF	diluted in 0.2% BSA in PBS (1:1000)
BSA	2% in PBS
Calpeptin	15 mg/ml in DMSO
CNTF	25 µg CNTF in 25 µl TRIS 5 mM (pH 8) diluted, stock solution: diluted to 10 µg/ml in 0.2% BSA in PBS, final concentration: diluted to 10 ng/ml in H2O
Dnase I	2000 U/mg, diluted in HBSS
Laminin	Stock solution: 1-2 mg/ml in TRIS-buffered saline, final concentration: diluted 1:1000 in distilled H2O
PBS	9,55 g PBS powder in 1000 ml H2O distilled, sterile filtered
PFA in PHEM	2.45 ml 8% PFA in PHEM 2.5 ml H2O distilled 50 µl Glutaraldehyde
PHEM	60 mM PIPES 25 mM HEPES 10 mM EGTA 2 mM MgCl2
PLO	Stock solution: 1 mg/ml in borate buffer, final concentration: diluted 1:10 in distilled H2O
Quenching solution	Glycine 100 mM, Ammonium chloride 100 mM; both diluted in PBS

Buffers and solutions	**Production**
TritonX-100	0.3% in PBS
Trypsin	diluted in HBSS to 25.000 U/ml

2.1.3 Culture media

Table 3: Used culture media and media production

Culture media	**Production**
CM with FBS (CM+)	FBS in CM (1:10)
CM with growth factors, but without FBS (CM0+)	BDNF and CNTF in CM (1:1000)
CMF media (Calcium- and magnesium-free)	H_2O distilled (450 ml)
	HBSS (10X, 50 ml)
	Sodium bicarbonate 7.5%, set to 7.4 pH
Cortex cell culture media (CM)	Neurobasal Medium (48.125 ml)
	Holo-Transferrin human (0.25 ml)
	PSN (0.5 ml)
	L-Glutamax (0.125 ml)
	B27 Supplement (1 ml)

2.1.4 Machines and software

Table 4: Machines and software

Machines and software	**Manufacturer**
Affinity Designer	Serif Ltd., West Bridgford, UK
Arium® pro H2O distilled Dispenser	Sartorius, Göttingen, Germany
Autoclave	Systec, Wettenberg, Germany
Bench (semi-sterile) Hera guard	Heraeus, Hanau, Germany
Bench (sterile) LaminAir HB 2448	Heraeus, Hanau, Germany
Binocular microscope	Zeiss, Jena, Germany
Cell culture pump	Schütt Labortechnik, Göttingen, Germany
Centrifuges 5415R, 5810R, 5415D	Eppendorf, Hamburg, Deutschland
Cohan-Vannas Spring Scissors (5.7 m)	FST (Fine Science Tools), Heidelberg, Germany
Dumont #5-Mirror Finish Forceps (11 cm)	FST (Fine Science Tools), Heidelberg, Germany
Fiji	NIH, Bethesda, MD, USA
Fluorescence light source	Zeiss, Jena, Germany

Machines and software	**Manufacturer**
Fluorescence microscope Axio Observer.Z1	Zeiss, Jena, Germany
Freezer -20°C	Bosch, Stuttgart, Germany
Freezer -80°C	Ewald, Rodenberg, Germany
GraphPad PRISM 9.4	GraphPad Software, Inc, San Diego, CA, USA
Ice Machine, Scotsman®	Frimont, Mailand, Italien
Imspector	Abberior, Göttingen, Germany
Incubation chamber, Incubator PM 2000 RBT	PeCon, Erbach an der Donau, Germany
Incubator for cell culture (37°C, 5% CO2)	Heraeus, Hanau, Germany
Measuring cylinders	Duran, Wertheim, Germany
Microsoft Office Excel 2016	Microsoft, Unterschleißheim, Germany
Microsoft Office PowerPoint 2016	Microsoft, Unterschleißheim, Germany
Microsoft Office Word 2016	Microsoft, Unterschleißheim, Germany
Motor-Pipette-Aid Accu-Jet® Pro	Brand, Wertheim, Germany
Neubauer Counting Chamber	Roth, Karlsruhe, Germany
Pipettes	Gilson, Villiers le Bel, France
Refrigerators	Liebherr, Biberach, Germany
REPLICATOR+ (3D-printer)	MakerBot Industries, Brooklyn, NY, USA
Rocking Device	NeoLab, Heidelberg, Germany
Roll mixer	Dynalab Corp., Rochester, NY, USA
STED microscope	Abberior, Göttingen, Germany
Tinkercad	Autodesk, San Rafael, CA, USA
Vortex Mixer SPROUT	Heathrow Scientific, Vernon Hills, IL, USA
Zen 2.5 (blue edition)	Zeiss, Jena, Germany

2.1.5 Consumables and expendables

Table 5: Consumables and expendables

Consumables and expendables	**Manufacturer**
Discharge Pipettes (5 ml, 10 ml, 25 ml)	Sarstedt, Nümbrecht, Germany
Falcon tubes (10 ml, 15 ml, 50 ml)	Sarstedt, Nümbrecht, Germany
Filters (sterile)	Sarstedt, Nümbrecht, Germany
FluoroDish (35 mm)	World Precision Instruments, Inc, Sarasota, FL, USA
Glass Pasteur pipettes	Sigma Aldrich, St. Louis, MO, USA
Parafilm	Pechiney Plastic Packaging, Menesha, WI, USA
Permanent marker (Lumocolor permanent S)	Staedtler, Nürnberg, Germany

Consumables and expendables	**Manufacturer**
Pipette tips (several sizes)	Sarstedt, Nümbrecht, Germany
Pipette tips with filter (several sizes)	Sarstedt, Nümbrecht, Germany
Round Device 450 µm (PDMS chip)	XONA microfluidics, Research Triangle Park, NC, USA
Safe-Lock tubes (0.5 ml, 1.5 ml, 2 ml)	Eppendorf, Hamburg, Germany
Scotch tape	Tesa, Hamburg, Germany
Sterile petri dish	Sarstedt, Nümbrecht, Germany
Syringe 20 ml (DiscarditTM II)	BD, Heidelberg, Germany
Templates for microscopy (3D-printed)	Custom made

2.1.6 Antibodies and staining reagents

Table 6: Antibodies and staining reagents

Antibodies and staining reagents	**Manufacturers**
βII-Spectrin	BD, Franklin Lakes, NJ, USA
βIII-Tubulin	Cell Signaling, Cambridge, UK
Alexa Fluor 594	Invitrogen, Waltham, MA, USA
Abberior STAR 635P	Abberior, Göttingen, Germany
Abberior STAR RED Phalloidin	Abberior, Göttingen, Germany

2.1.7 Viral vectors

See section 2.2.1

2.2 Methods

2.2.1 Viral vectors

A recombinant adeno-associated viral vector (AAV1/2) was used for all experiments, expressing enhanced green fluorescent protein (EGFP; **Figure 5**) for labeling of neurons. An AAV pseudotype was chosen to increase transduction efficiency, consisting of AAV1 inverted terminal repeats (ITR) packed into the capsid of the AAV2 serotype. The vector "pAAV-9(5)hSyn-EGFP-CytbAS-ohne-Not" (AAV.EGFP; GenBank: HQ416702.1) expressed EGFP, driven by a human synapsin-1 promoter and a human h1 promoter, as described before (Koch et al. 2011), kindly gifted by Uwe Michael, Göttingen. AAV production was performed as described by Zolotukhin et al. (1999). The virus was employed at DIV 4 with a titer of 0.5 x 10^7 transduction units (TU) per chamber into the soma compartment. In general, a transduction rate of > 90% was achieved, with no major toxicity.

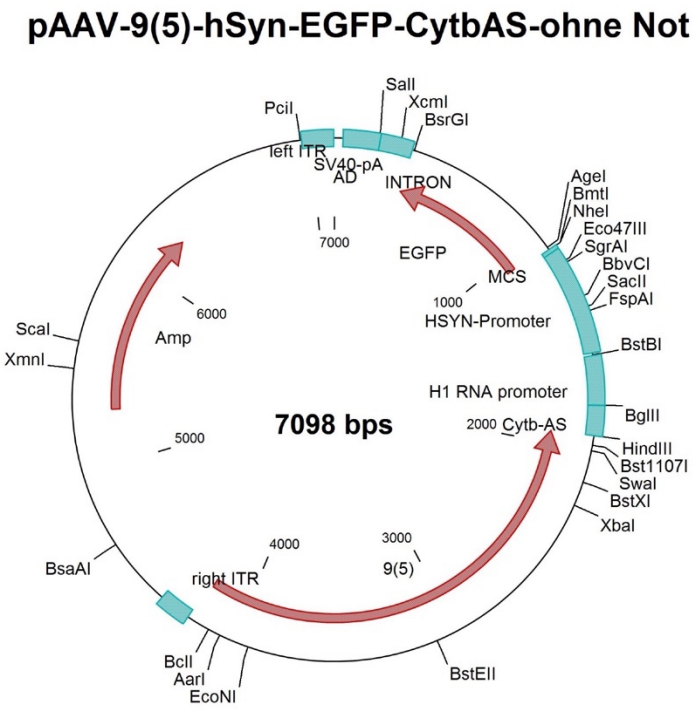

Figure 5: Sequence of AAV.EGFP. The adeno-associated viral vector of the pseudotype AAV1/2 expresses EGFP. Expression is driven by a human synapsin-1 promoter and a human h1 promoter, as described before (Koch et al. 2011). The figure was used with the kind permission of Prof. Dr. Uwe Michel, Göttingen.

2.2.2 Cell culture

2.2.2.1 Coating of tissue culture dishes

Sterile tissue culture dishes (FluoroDishes) were coated with poly-L-ornithine (PLO) and laminin. PLO was diluted at 1:10 in sterile H_2O. Therefore, tissue culture dishes were filled with 1 – 2 ml of diluted PLO and were incubated at room temperature for at least 3 h. The fluid was then removed using a cell culture aspiration pump, and the dishes were washed twice using sterile H_2O. For laminin coating, laminin was diluted at 1:1000 in sterile H_2O. Dishes were then filled with 1 – 2 ml of diluted laminin and were incubated overnight in a cell incubator (37°C, 5% CO_2). The remaining fluid was removed, and dishes were washed twice using sterile H_2O. Dishes were then placed under a laminar flow hood to dry before assembling with a polydimethylsiloxane (PDMS) chip.

2.2.2.2 Preparation of microfluidic chambers

Microfluidic chambers (MFC) were used to separate axons from soma and dendrites for the isolated analysis of axons, as previously described (Taylor et al. 2005). MFCs are PDMS chips with two compartments, connected by 450 µm long and 3 µm thin tunnels, the microgrooves. After the preparation of MFCs, neurons can then be seeded into the first compartment (soma compartment). During culture, neurons extend dendrites and axons

towards the microgrooves. Because axons grow faster and longer than dendrites, only axons cross the 450 µm long microgrooves and reach the second compartment, the axonal compartment (Taylor et al. 2005). This method allows for the isolated analysis of axons.

To assemble MFCs, PDMS chips were freed from dust using scotch tape. The chambers were then submerged in a sterile petri dish filled with 70% undenatured ethanol for 10 min for sterilization. Afterward, the chambers were placed in a laminar flow cabinet for at least 3 h to dry. The dried chambers were then mounted onto 35 mm tissue culture dishes, pre-coated with PLO and laminin (see 2.2.2.1), using a sterilized forceps. To improve adhesion, gentle pressure onto the upper side of the PDMS chip was applied using sterile gloves. The soma compartment was then marked using a permanent marker for easier identification. Afterward, the soma compartment was loaded with 200 µl of cortex cell culture media (CM). Therefore, the pipette tip was carefully placed proximal to the main channel entrance, and media was released with pressure until a drip appeared on the opposing side of the main channel. Chambers were then placed in an incubator (37°C, 5% CO_2) overnight to allow the media to flood the microgrooves. The axonal side was prepared the following day likewise. Chambers were then placed in an incubator until cell preparation.

2.2.2.3 Preparation of cortices

The use of E18 Wistar rat embryos for the isolation of cortical tissue was carried out in accordance with the approved experimental animal licenses (33.9-42502-04-11/0408) issued by the responsible animal welfare authority (Niedersächsisches Landesamt für Verbraucherschutz und Lebensmittelsicherheit). Experiments were overseen by the University Medical Center Göttingen's local animal welfare committee. Only trained and authorized personnel were used to conduct the animal experiments.

The preparation of cortices was based on a protocol published by Sahu et al. (2019). Therefore, pregnant E18 rats were euthanized using CO_2. A solution of 70% ethanol was used afterward to disinfect the abdomen. The abdomen was cut using a surgical scissor, and the uterus was removed. Immediately the uterus was placed in a dish with cold (4°C) CMF media (calcium- and magnesium-free, to prevent the inactivation of trypsin and to flush chelators out of culture). The uterus was then opened, and the embryos were removed. Afterward, the heads of the embryos were dissected and transferred into another dish. The scalp was removed using a binocular microscope and microsurgical instruments, and the skullcap was cut along the *sutura sagittalis*, and then folded back. The brain was then removed using a forceps, and the pons was flipped over and removed. The brain hemispheres were then turned over and dissected using a scissor. For the reduction of fibroblast contamination, the meninges were carefully removed using forceps without damaging the brain tissue. Afterward, the cortices were dissected using a scissor and transferred into a 10 ml falcon tube containing CMF.

2.2.2.4 Preparation of neurons

To isolate cells from the tissue, the supernatant was removed, and 1 ml of trypsin was added to the tube. The falcon tube was then incubated at 37°C for 14 min in a water bath. After 10 min, 50 µl of Deoxyribonuclease I (DNAse) was added. After incubation, tubes were centrifuged for 1 min at 800 rounds per minute (RPM) at room temperature, and trypsin was removed using a pipette. Afterward, the pellet was resuspended in 1 ml of fetal bovine serum (FBS) and was then carefully triturated five times using a 1 ml pipette tip. After waiting for 1 min, the supernatant was transferred into a 15 ml falcon tube. To further homogenize the remaining tissue, 1 ml of cortex cell culture media containing FBS (CM+) and 50 µl of DNAse was added, and the tissue was then triturated five times using a narrowed glass Pasteur pipette. The supernatant was again transferred into the 15 ml tube and centrifuged for 4 min at 800 RPM at room temperature. The supernatant was removed, and the pellet was then resuspended in 500 µl of CM+. The number of cells in the suspension was then calculated using a Neubauer counting chamber.

2.2.2.5 Seeding of neurons

To prepare MFCs for the seeding of neurons, media was changed to fresh CM in both compartments. The media was then carefully aspirated from the soma compartment using a cell culture aspiration pump. A total of 5 µl of cell suspension (containing 6000 cells per µl) was added into each of both wells of the soma compartment. Therefore, the pipette tip was inserted close to the main channel entrance, and the cell suspension was released with pressure. A final concentration of 60.000 cells per chamber was achieved. To allow cells to attach to the cell culture dish, chambers were placed in the incubator for at least 1 h. After 1 h, 200 µl of CM+ was carefully added into the soma compartment.

2.2.2.6 Cell culture maintenance

For the preparation of the culture media CM, CM+, CM0+, and CM++, see **Table 3**. Fluids were added into a sterile flask (500 ml) and then filtered through a sterile filter (pore size 0.2 µm) into a second sterile flask. For CM+, sterile filtered FBS was added in a 1:10 ratio. For CM0+, 1:1000 of ciliary neurotrophic factor (CNTF) and 1:1000 of brain-derived neurotrophic factor (BDNF) were added to CM. For CM++, 1:1000 of CNTF and 1:1000 of BDNF were added into CM+. All culture media were stored in a fridge and were preheated to 37°C before use.

Half of the media in a MFC was changed every 2 to 3 days. Therefore, media was removed almost entirely from one well of the soma and the axonal compartment. Then, 90 µl of fresh media was gently added into the opposing well of the soma compartment. In the axonal compartment, 60 µl of fresh media was added into the opposing well, creating a gradient towards the axonal compartment. The gradient was omitted after DIV 7 to prevent glial cell migration through the microgrooves. CM+ was used from DIV 0 – 4, CM++ was used from

DIV 4 – 6, and CM0+ was used from DIV 6 – 11. FBS was omitted after DIV 6 in order to prevent glial cell overpopulation.

2.2.2.7 Administering of viral vectors or calpeptin into the MFCs

For virus transduction, almost all media from both wells of the soma compartment was removed. Quickly, 100 µl of media containing virus or drug was added into one well. After the fluid started to fill the opposing well, 20 µl of old media was removed from the opposing well. Again 100 µl of media containing virus was added into the first well. In the axonal compartment, virus was administered likewise, or media was changed as previously described.

For inhibition of calpain in axons, calpeptin in DMSO (Dimethyl sulfoxide) or DMSO alone as a control were used. First, media was changed in the soma compartment. After the removal of media from the axonal compartment, media containing calpeptin (10 µM) in DMSO or DMSO alone (both diluted to 0.012% in media) were added into the axonal compartment. If 200 µl of media was administered into the soma compartment, 150 µl of media containing calpeptin in DMSO or DMSO alone were added to the axonal compartment to create fluidic isolation of the axonal compartment through a volume gradient. Axons were incubated with calpeptin in DMSO or DMSO alone for 1 h before the axotomy.

2.2.2.8 Axotomy

To induce axonal regeneration, axons were dissected through vacuum aspiration axotomy, as described previously (Taylor et al. 2005). To perform axotomy, media was changed in the soma compartment as described above. A glass Pasteur pipette was attached to a cell culture pump, set at 75 mmHg. Using the Pasteur pipette, media was aspirated from one axonal well until an air bubble passed through the main channel, dissecting the axons, as **Figure 6** shows. Then, 110 µl of media was added quickly with pressure until a drip appeared on the opposing side of the main channel. Afterward, the axotomy was repeated in the opposing axonal well. In total, axotomy was performed 2 – 6 times per chamber. The axonal compartment was then filled with 150 µl of media. Successful axotomy was confirmed using a standard cell culture light microscope. The axotomy was routinely achieved at around 30 µm away from the microgrooves in the axonal side.

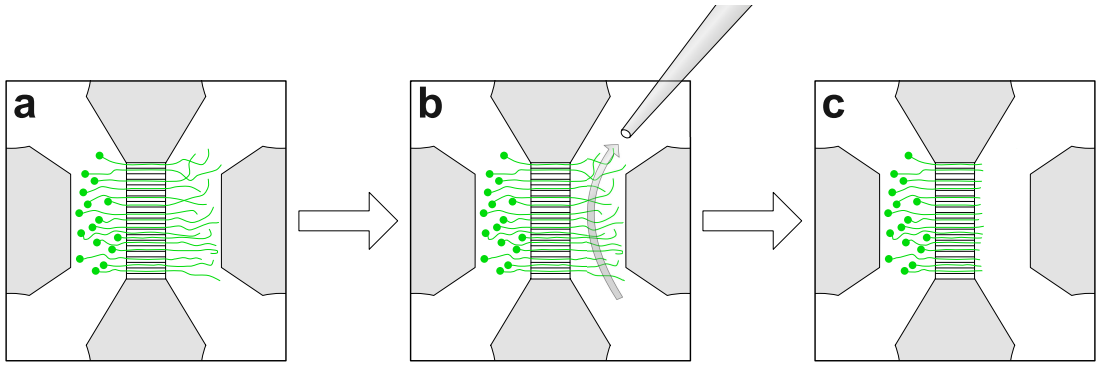

Figure 6: Graphical explanation of axotomy procedure. As it can be seen in **(a)**, axons pass through the microgrooves before the axotomy. Using a glass Pasteur pipette (depicted as a grey tube), media is aspirated from one well of the axonal compartment **(b)**. Afterward, 150 µl of media is resuspended into the well (not shown). After 2 – 4 rounds of axotomy, axons are routinely cut at around 30 µm distance from the microgrooves **(c)**.

2.2.2.9 Fixation

For the fixation of chambers, almost all media was removed from all wells. Chambers were then washed by adding sterile phosphate-buffered saline solution (PBS), containing 1:100 penicillin-streptomycin-neomycin antibiotic mixture (PSN) to one side of both compartments. PBS was then removed from the opposing well using a plastic transfer pipette; the process was repeated three times. PBS was then completely removed from all wells. Cells were then fixed using pure methanol or paraformaldehyde (PFA; 4% in PHEM (see **Table 2**) containing 1% glutaraldehyde). In the case of methanol fixation, methanol, precooled to -20°C, was added three times, and chambers were placed at -20°C for 10 min. PFA was added three times, and chambers were incubated at room temperature for 1 h. Methanol or PFA was then completely removed, and chambers were washed three times with PBS. Chambers were then stored at 4°C until immunocytochemistry was performed.

2.2.3 Immunocytochemistry

To visualize βIII-tubulin, βII-spectrin, and F-actin, immunocytochemistry was performed. Therefore, all fluid was removed from fixed chambers, and cells were washed one time with sterile PBS. Afterward, all PBS was removed from all wells. PFA-fixed cells were quenched using quenching solution for 5 min at room temperature. To improve the penetration of antibodies into the cells by permeabilization of the cell membrane, Triton X100 (0.3% in PBS) was added for 5 min. Chambers were then washed three times with PBS. Afterward, cells were blocked for 20 min at room temperature with bovine serum antigen (BSA), to block the unspecific binding of the antibodies (2% in PBS). Then, fluid was removed from both axonal and one soma compartment, and primary antibodies (200 µl) were added into one well of the axonal side. Chambers were then incubated for 1 h at room temperature. Afterward, the fluid was again removed completely, and chambers were washed gently three times with PBS for 5 min on a shaker. For secondary antibody or phalloidin administration,

fluid was again removed, and secondary antibodies were added into one well of the axonal side. Chambers were then incubated again for 45 min at 37°C. The antibody solution was then removed, and chambers were washed gently three times for 5 min in PBS on a shaker. Chambers were then stored at 4°C under light protection until STED microscopy was performed.

2.2.4 Microscopy techniques

2.2.4.1 Manufacture of custom-made microscopy template

To position and stabilize the MFC inside the incubation chamber (IC) of the microscope and seal the IC against heat- and CO_2-loss, a custom-made 3D-printed microscopy template was manufactured. Therefore, the diameter of the MFC and the IC were measured, and a plate, fitting inside the IC, was designed using the online 3D-modeling program Tinkercad. A circular shape with the dimensions of the MFC was then subtracted from the plate, creating a hole. To ensure improved insertion of the MFC into the template, the edges of the hole were tilted. The 3D-model was then exported and printed at the "Bereichsbibliothek Medizin Göttingen", using the 3D-printer REPLICATOR+.

2.2.4.2 Identification of regenerating neurons

To determine whether an axon is regenerating after axotomy or is just crossing the microgrooves for the first time, the axons were imaged using an inverted fluorescence microscope (Axio Observer.Z1). Images were taken 20 min before the axotomy, 5 min after the axotomy, and 2, 3, 4, 5, or 6 h after the axotomy, right before the fixation. In detail, the chambers were placed into the IC of the microscope (preheated to 37°C, at 5% CO_2) in a custom-made 3D-printed template (see 2.2.4.1) to prevent loss of heat and CO_2. Using light and fluorescence microscopy, images with 20x magnification of the axonal compartment proximal to the microgrooves were acquired. The side of the MFC where the microgrooves ended leveled was chosen as the first picture. Using the microscopy software Zen 2.5 (blue edition), the axonal end of the microgrooves was set to be 150 µm apart from the left side of the image. The image was then acquired using automatic exposure and lighting parameters. The following 8 microgroove endings were then imaged with an overlap of 1 microgroove. 5 – 10 pictures were taken per chamber. To identify regenerating axons, axons with growth cones in the final picture of the time series were marked with a red arrow using the Zen editing tool. The microgrooves in every image were then consecutively numbered, starting at the first leveled microgroove. To identify an axon as regenerating, marked axons in pre-fixation images were compared to images of the same microgrooves acquired before and 5 min post-axotomy using the "Multiview" tool. Therefore, images of the same region of the three time points were loaded into the multiview panel, and the pictures were aligned according to the microgrooves. Using the position marker, it was then examined whether a GC or axon visible in the post-axotomy image was also visible before the axotomy. GCs that

were not visible in the other frames were classified as regenerating. It was also examined whether an axotomy had been sufficient or not. Only regenerating axons following a sufficient axotomy were chosen for STED microscopy and were marked.

2.2.4.3 STED microscopy

For the acquisition of two-color STED images, a quad scanning STED microscope, located at the "Max-Planck-Institut für Multidisziplinäre Naturwissenschaften (Faßberg-Campus)" was used, equipped with an UplanSApo 100x/1.40 Oil objective and 488 nm, 561 nm, and 640 nm pulsed excitation lasers. The platform was an IX83 Olympus microscope, that was equipped with a 4-color light-emitting diode (LED) illumination source and a monochrome widefield camera, with a ½" charge-coupled device(CCD)-chip, and 1280x960 pixels. For STED imaging, Alexa Fluor 594 was excited at 561 nm (at 95% power). Abberior STAR 635p and Abberior STAR RED were excited at 640 nm (at 3% and 16% power, respectively), and STED was performed at a wavelength of 775 nm (at 40% power) and 3000 mW at a repetition rate of 40 Mhz. A pixel size between 20 and 25 nm was used. The dwell time was set to 10 µs, and the pinhole was set to 0.6 – 1.0 airy units. Images were saved as multi-sensor rack file format (MSR) files.

2.2.5 Analysis of microscopy data

2.2.5.1 Image processing

To convert MSR files into tagged image format files (TIFF), a macro for the open-source freeware Fiji (Schindelin et al. 2012) was used. The Fiji plugin "MosaicJ" (Thévenaz and Unser 2007) was used to create montages of axons extending over several images. The images were arranged, and mosaics were created upon deactivation of the functions "Smart Color Conversion", "Blending", and "Rotation", to preserve the original data. The final mosaic was then converted back to 8-bit and saved.

2.2.5.2 Analysis of STED images

To detect morphological changes on a nanoscale level and to assess periodicity, obtained images were analyzed using Fiji. Images of different stains for cytoskeletal proteins were analyzed independently. To evaluate the morphology of GCs (including length, width, and area), the border of the GC was traced using the "polygon selection" tool. GC length was analyzed by using the "straight line" tool to draw a line from the GC base to the GC's tip. The width was determined by measuring the widest straight within the GC, orthogonal to the length of the GC. To measure the length of the axonal segment and to plot a line intensity curve, a segmented line with spline fit was drawn from the GC tip towards the axotomy border. The line thickness was set to cover the width of the narrowest part of the axon, typically at or close to the axotomy border. To reduce data size and outliers in intensity plot

scans, the measurements were summarized for every 1 µm and normalized to each dataset's maximum to allow for comparison between different axons, using Microsoft Excel.

To evaluate changes in βII-spectrin periodicity and axonal diameter, the axon was divided into 10 µm segments. This was done by using a self-programmed macro for the segmentation of nonlinear structures, named "Segmenter" (see code in 6.1). Changes in axonal diameter were measured along the axon for every 10 µm, starting from the GC neck, by measuring axon thickness in tubulin stains using the "straight line" tool. βII-Spectrin periodicity was calculated by measuring the length of every periodic patch in a 10 µm segment and dividing the total length by 10 µm. The average patch size and the number of periodic patches per segment were also assessed.

One periodic patch was defined as an array of at least three individual βII-spectrin signals inside the axon with a periodic distance of 150 – 250 nm between the signals. This periodicity was assessed by drawing a line across the periodic patch and creating an intensity plot, confirming the periodic distance of intensity peaks. This was performed in both non-axotomized and axotomized axons. The first 250 µm of the axon, starting at the GC base, were considered for non-axotomized axons. Average spectrin tetramer spacing was analyzed by plotting intensity line scans along periodic patches at multiple axons at distances of 0, 100, and 200 µm from the GC and measuring the distance between signal peaks.

To enhance the visibility of actin in co-stainings of actin and spectrin (**Figure 11** and **Figure 12**), actin was pseudo-colored using the CET-L15 colormap by Peter Kovesi (2015) (colorcet.com). To analyze the position of spectrin and actin intensity peaks along the GC, line intensity scans for actin and spectrin were performed along the GC. The absolute intensity peak distances from the GC were noted, as well as the relative position inside the GC by dividing by the individual GC length.

2.2.5.3 Analysis of axonal outgrowth speed

Time-lapse microscopy previously captured for a different experiment (manuscript in preparation) was used to assess the axonal outgrowth speed. Therefore, cells were cultured as described above and fixed on DIV 10. Time-lapse videos of 10-minute length were captured before the axotomy, 5 min after, and 2, 4, and 6 h after the axotomy. To determine the outgrowth speed, the position of the GC tip at the first and the last frame of the video was marked, and the distance was measured using Fiji and divided by 10 min.

2.2.5.4 Analysis of the effect of calpeptin on axonal outgrowth and regeneration

To evaluate the effect of calpeptin on axonal regeneration, images captured for the identification of regenerating axons (see 2.2.4.2) were analyzed. Therefore, the number of regenerating axons per nine microgrooves was counted in chambers treated with calpeptin or DMSO. At 20x magnification, nine microgrooves could be seen in one image. To evaluate

the effects of calpeptin on the outgrowth length of regenerating axons, the length of the regenerating axons was measured using the "segmented line measurement" tool of Zen 2.5.

2.2.6 Statistics

All statistical evaluation was done using the Prism 9.4 software. Student's t tests (two-tailed) were used to compare two groups. Kolmogorov-Smirnov or non-parametric Mann-Whitney U tests were used in case the assumptions for the t test were not met. To compare more than two groups, one-way analysis of variance (ANOVA) was used and was followed up by Dunnett's multiple comparisons test. Estimated curve fits were created using GraphPad Prisms' sixth-order polynomial nonlinear fit function. In general, mean values ± SEM are described unless otherwise noted. Whenever possible, individual data points were shown in graphs for greater transparency. At least three independent experiments were analyzed for each experiment unless otherwise noted. To visualize significant differences between compared groups the following asterisks were used: * $p < 0.05$, ** $p < 0.01$, *** $p < 0.001$, **** $p < 0.0001$. Graphical illustrations were designed using Affinity Designer and Microsoft Office PowerPoint 2016. 3D-models were designed using Tinkercad. All graphs or illustrations originally published by Hofmann et al. (2021; 2022) were used and or modified under [Copyright: CC BY 4.0].

3 Results

3.1 Axonal outgrowth

3.1.1 Distribution of cytoskeletal proteins along the axon and the growth cone

3.1.1.1 Spectrin and tubulin

To allow for isolated analysis of axons, primary rat embryonic cortical neurons were cultured in compartmentalized MFC in all experiments (see 2.2.2.2). Neurons were planted in the soma compartment and stretched their axons through the microgrooves to the axonal compartment (**Figure 7**).

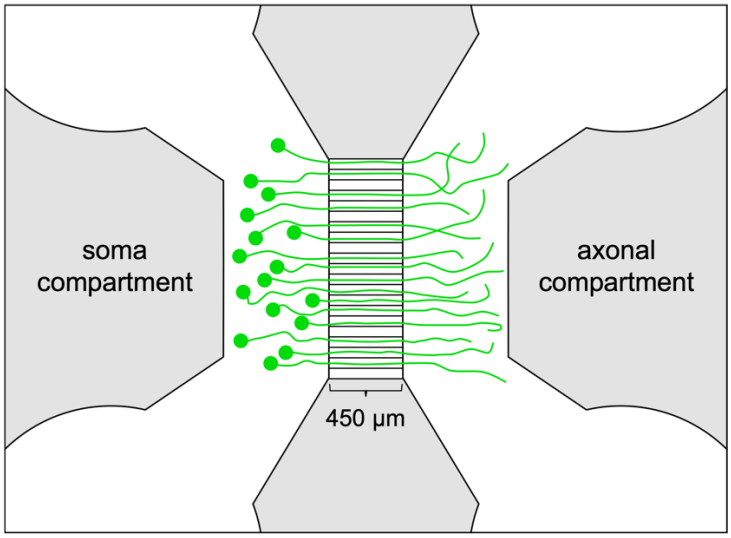

Figure 7: Schematic depiction of a microfluidic chamber seeded with primary cortical neurons. The green color resembles the transduction of neurons with an AAV.EGFP virus (see section 2.2.1). Neurons are seeded into the soma compartment (to the left). During culture, axons extend and cross the 450 µm long microgrooves, dendrites, however, do not extend far enough to cross this distance. Axons are, therefore, isolated in the axonal compartment (to the right).

The cells were fixed on DIV 11 (when axons typically traversed the microgrooves and entered the axonal compartment), immunostained against different cytoskeletal proteins, and analyzed using STED microscopy.

The first experiment aimed to study the general spatial distribution of important components of the axonal cytoskeleton along the GC and the non-axotomized axon. Therefore, 50 µm long intensity line scans for spectrin and tubulin along the GC and the adjacent axon were analyzed (**Figure 8**).

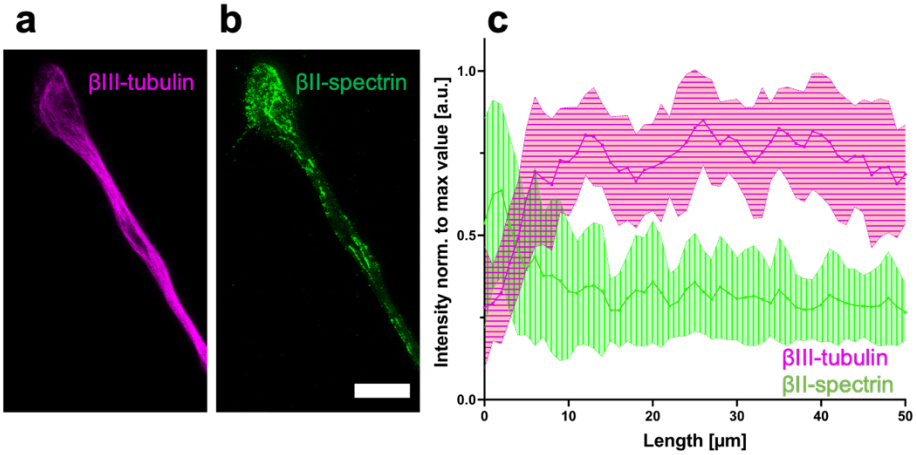

Figure 8: Distribution of tubulin and spectrin along the axon. (a-b): Representative STED images of an axon stained for spectrin and tubulin. Cells were fixed on DIV 11. Spectrin is enriched in the GC, while tubulin concentration is decreased. The scale bar is 5 µm. **(c)**: Quantification of 50 µm long line intensity scans along the axon, starting from the GC base (to the left). While the tubulin signal is weaker in the growth cone compared to the axon, the intensity of the spectrin signal peaks in the growth cone. Data is shown as mean ± SD. At least 5 biological replicates were analyzed, and 11 axons were analyzed in total.

The intensity of tubulin was highest along the axon and significantly reduced in the GC by almost 40% (Axon: 0.75 ± 0.02 vs. GC: 0.44 ± 0.04, see **Figure 9**). In contrast, spectrin showed the highest concentrations in the GC and was 40% less abundant along the axon (GC: 0.5 ± 0.04 vs. Axon: 0.3 ± 0.04). These results imply that, in contrast to tubulin, spectrin is substantially enriched in the GC and is integrated into the axonal cytoskeleton at a lower concentration.

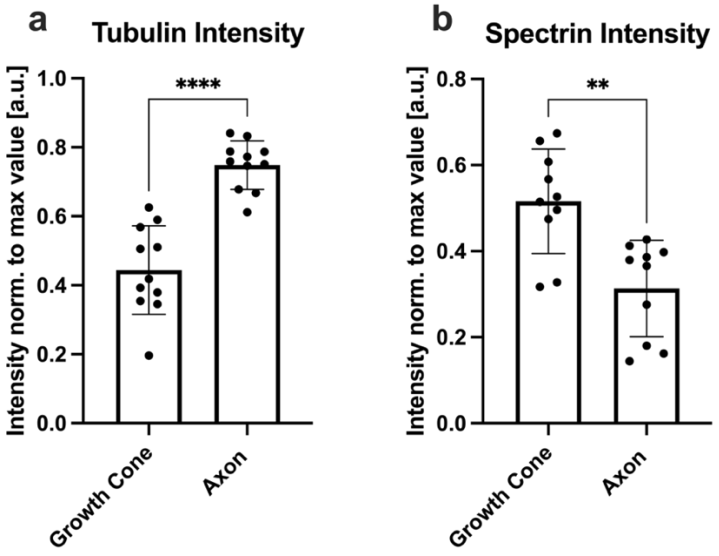

Figure 9: Quantified distribution of tubulin and spectrin along the axon. Analysis of 50 µm long line intensity scans along the axon, starting from the growth cone tip. Cells were fixed at DIV 11 and stained for tubulin and spectrin. Due to the mean growth cone length, the GC is represented by the first 7 µm of the line intensity scan, while the axon is represented by the remaining 7 – 50 µm. While the βIII-tubulin signal is lower in the GC than the axon **(a)**, the βII-spectrin-fluorescence intensity peaks at the growth cone **(b)**. Data is displayed as mean ± SD. There were at least 5 biological replicates examined and 11 axons in total.

F-Actin is known to be highly enriched in the GC. To study how the enrichment of spectrin in the GC was related to the presence of F-actin, qualitative co-stainings of spectrin and F-actin were obtained using STED microscopy (for staining details, see 2.2.3). To measure the relative location of spectrin and actin inside the GC, line intensity scans were performed along the GC.

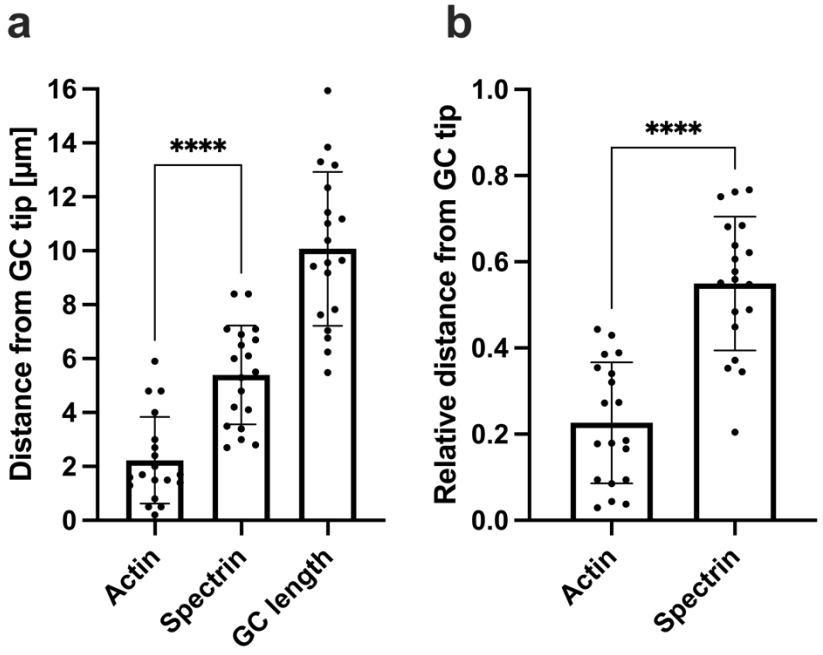

Figure 10: Localization of actin and spectrin fluorescence intensity peaks inside the GC. Quantification of spectrin and actin line intensity scans along the GC beginning at the growth cone tip, including filopodia. Cells were fixed at DIV 11 and stained for actin and spectrin. Intensity measurements were averaged for every 200 nm, and the spacing between each peak's maximum intensity and the GC tip was recorded. The measured GC lengths are additionally shown in **(a)**. **(b)** displays the spacing between the spectrin and actin intensity peaks with regard to the length of each individual GC. Spectrin signal peaks farther from the GC tip than the actin signal does. A minimum of two biological replicates and a total of 19 GC were examined.

Figure 10 shows the location of the enrichment of spectrin relative to the enrichment of actin and the GC length. Spectrin intensity peaks in the approximate middle of the GC, this region corresponds to the central region of the GC (Actin: 2.2 µm ± 0.4 µm, Spectrin: 5.4 µm ± 0.4 µm). The analyzed GCs had an average length of around 10.1 µm ± 0.7 µm, including filopodia. Therefore, the peak of spectrin intensity was indeed in the approximate middle of the GC, at around 3 µm from the actin intensity peak and around 5.4 µm afar from the tip of the GC, which can be seen in **Figure 11**.

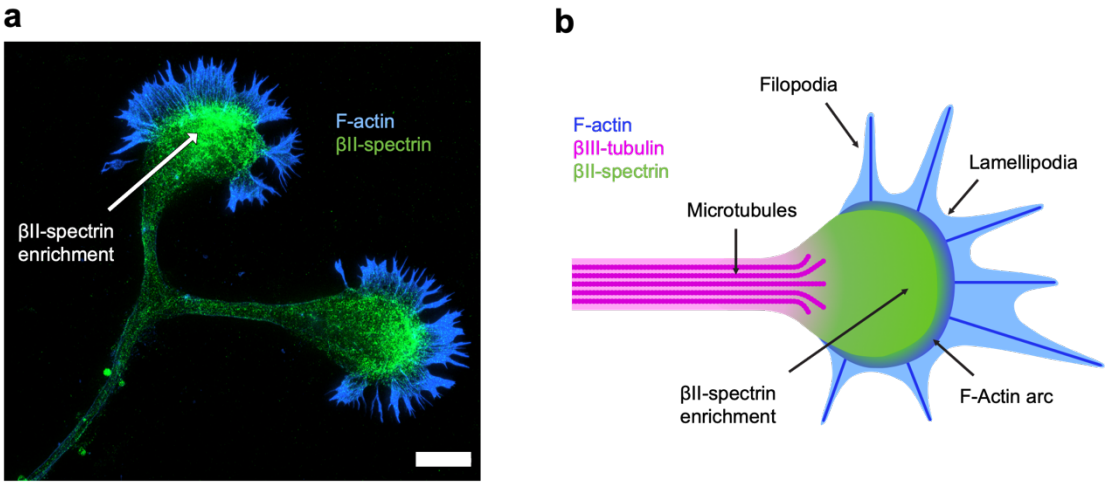

Figure 11: Relation of F-actin and spectrin in the axonal growth cone. (a): Growth cone stained for spectrin and F-actin in a typical STED image. Cells were fixed on DIV 11. Spectrin molecules are enriched close to actin filaments. The scale bar is 5 µm. **(b)**: A growth cone is depicted schematically, with the central zone indicating an enrichment of II-spectrin. The axon shaft is formed by microtubules that splay into the GC base. An F-actin arc, lamellipodia, and filopodia extend from the edge of the GC.

Figure 11, **b** provides a schematic display of the relationship of tubulin, spectrin, and F-actin in the GC. The spectrin signal frequently colocalized with actin and was often increased particularly near the base of F-actin bundles. Representative micrographs are shown in **Figure 12**. This enhancement could suggest a stabilizing or anchoring function of spectrin for the outgrowing actin filaments in GCs.

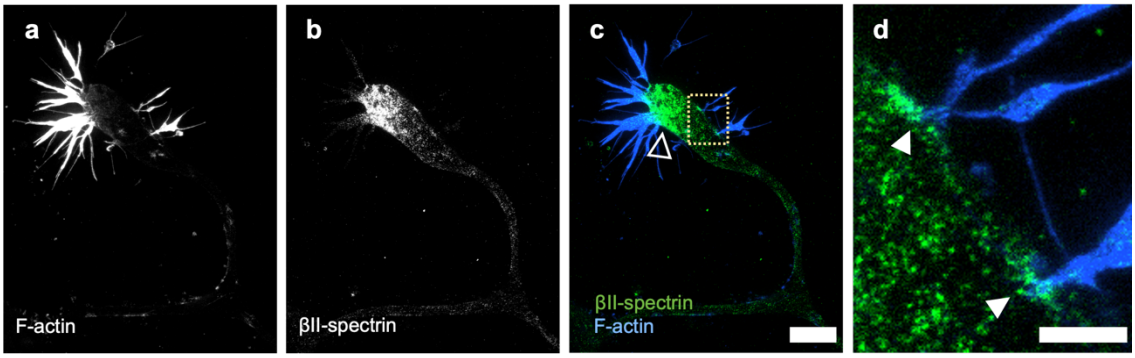

Figure 12: Representative STED image of an axonal growth cone stained for F-actin and spectrin. Cells were fixed on DIV 11 and were imaged using STED microscopy. Spectrin is more abundant in the axonal growth cone, often around the base of filopodia (marked by an open arrowhead). F-actin filopodia are stained in **(a)**, spectrin enrichment in the GC can be seen in **(b)**. **(c)** shows the composite image of **(a)** and **(b)**. **(d)** depicts an enlarged version of **(c),** filled arrowheads mark enriched spectrin signals at the base of filopodia. The scale bar is 4 µm in **(a-c)** and 1 µm in **(d)**.

3.1.2 Development of MPS

3.1.2.1 MPS development in non-axotomized axons

Understanding how the MPS develops in the youngest part of the axon, the segment adjacent to the GC, is essential for comprehending the process of MPS development in a growing axon in general. Therefore, the first 250 µm of the axonal segment close to the GC were analyzed for the presence of MPS. As shown in the representative micrograph in **Figure 13**, the axonal segment closer to the soma shows spectrin periodicity, while the segment closer to the GC shows none.

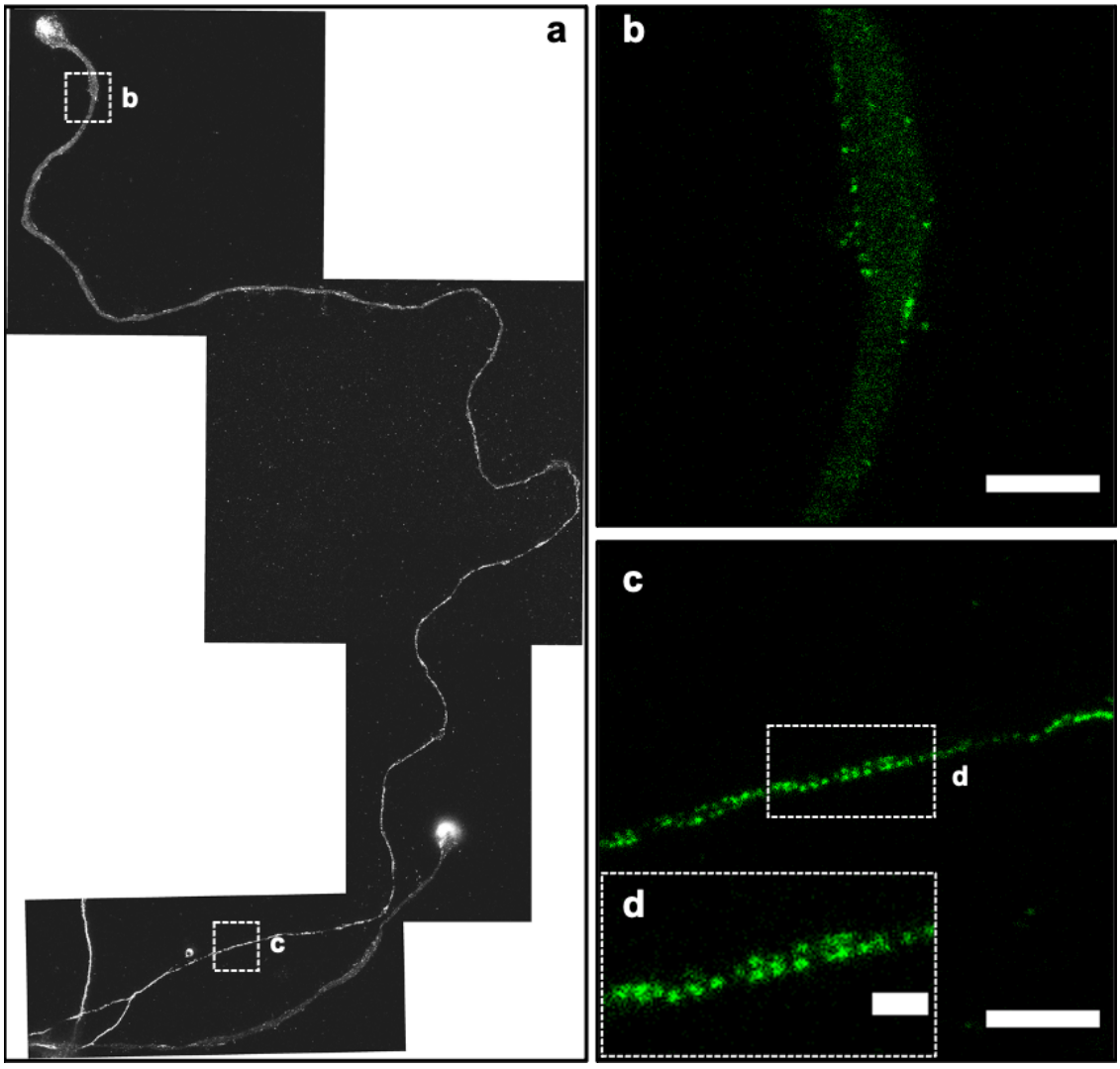

Figure 13: Representative image of MPS development in an axon stained for spectrin. Cells were fixed on DIV 11 and were imaged using STED microscopy. **(a)**: Axon stitched from multiple images, the GC and 300 µm of axon towards the soma can be seen. **(b)**: Enlarged section of the axon, with no periodicity visible at 10 µm away from the growth cone. The scale bar is 2 µm). **(c)**: Enlarged section of the axon, 270 µm from the growth cone. The scale bar is 2 µm. **(d)**: Enlarged section of **(c)**, MPS is clearly visible. The scale bar is 0.5 µm.

To quantify the MPS development, the axon was divided into 10 µm segments, and the length of axon showing periodic spectrin patterns per segment was evaluated. From the

axonal GC base up to 250 µm towards the soma, there was a consistent, nearly 10-fold increase in axonal spectrin periodicity (first 10 µm: 7.5% ± 2.4%, 250 µm from GC: 68.5% ± 16.5%), as shown in **Figure 14**.

At around 220 µm from the GC, 50% periodicity was reached (5 µm of 10 µm measured axon at that distance were periodic), corresponding to a maturation time of 12 h in the present culturing conditions (see 3.2.1.4 for measured outgrowth speed). At distances of 250 – 350 µm from the GC, a mature MPS (10 µm of 10 µm measured axon at that distance were periodic) was observed (data not shown). These distances resemble a maturation time of approximately 14 – 19 h until an axonal segment displays a fully periodic MPS.

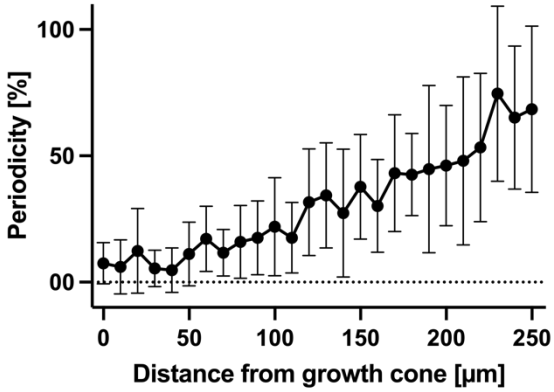

Figure 14: Development of periodicity over the length of the axon. Cells were fixed on DIV 11, axons were stained for spectrin, and were imaged using STED microscopy. Periodicity increases linearly towards the soma. The data is displayed as mean ± SD. At least 5 biological replicates were examined with a total of 11 axons. Not all axons could be included at distal points due to difficulties in tracking them back for long distances.

3.1.2.2 Periodic patches are the building blocks of MPS formation

Spectrin periodicity in growing axons did not extend continuously from proximal to distal but developed in the distal axon from multiple single periodic spectrin patches that extended and coalesced towards the soma, as shown in **Figure 15**. A "periodic spectrin patch" was defined as a continuous array of at least 3 spectrin-fluorescence signals inside the axon with a mean periodic distance of not more than 150 – 250 nm.

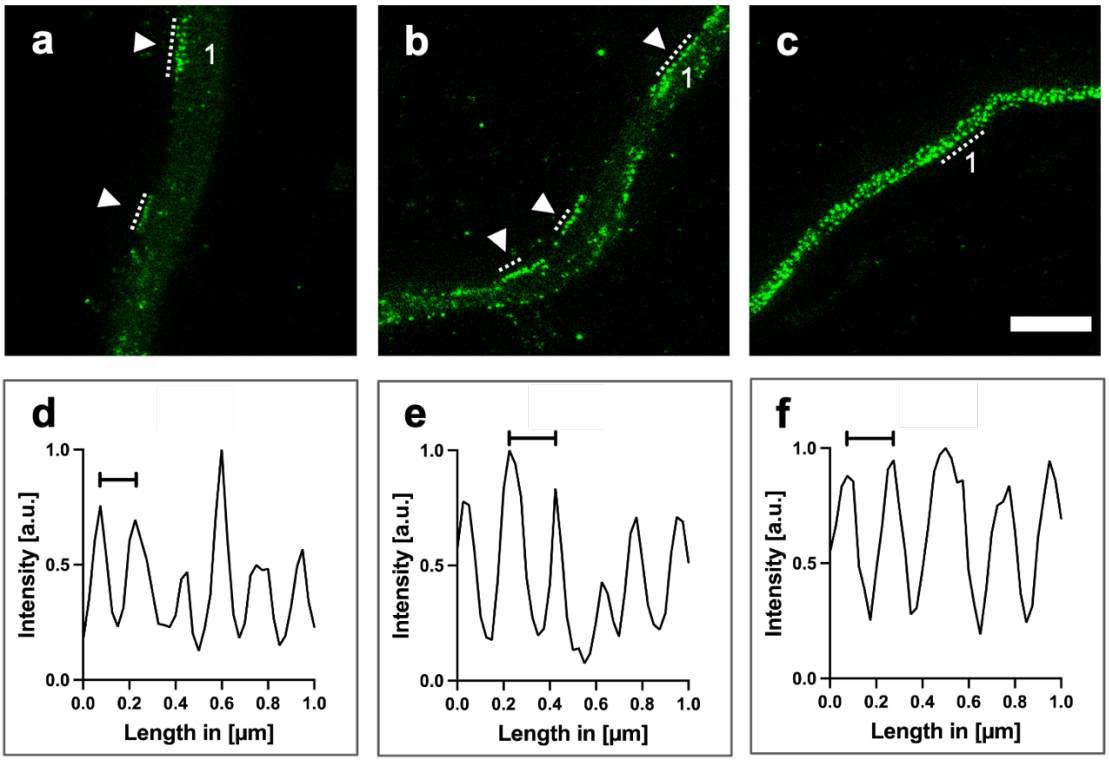

Figure 15: Different stages of MPS development in different sections of the axon. Cells were fixed on DIV 11, axons were stained for spectrin, and were imaged using STED microscopy. **(a)**, **(b)**, and **(c)** are 30 µm, 170 µm, and 260 µm afar from the GC, respectively. Periodic patches are indicated by arrowheads. The scale bar is 2 µm. **(d)** shows a line intensity plot of **(a).** The marked distance resembles 150 nm. **(e)** shows a line intensity plot of **(b).** The marked distance resembles 200 nm. **(f)** shows a line intensity plot of **(c).** The marked distance resembles 200 nm.

To quantify the role of periodic patches in MPS development, every periodic patch along the axons already analyzed for periodicity development evaluation was analyzed again. Therefore, for each 10 µm long axonal segment, the number and length of these periodic spectrin patches were measured along the growing axon. In the first 100 µm of axon next to the GC, short periodic spectrin patches were seen at a density of around 1 patch per 10 µm of measured axon (1.1 ± 0.1). Between 100 – 200 µm from the GC, the periodic patch density increased to 2 patches per 10 µm (2.1 ± 0.1). At distances of more than 200 µm from the GC, periodic patch density slowly decreased again, as single periodic patches enlarged and coalesced (at 250 µm: 1.8 ± 0.6; see **Figure 16, a**).

In the first 100 µm next to the GC, the average length of periodic spectrin patches was 0.6 µm (644 nm ± 96.4 nm), equivalent to three consecutive spectrin tetramers. The length of the periodic spectrin patches increased gradually between 100 – 200 µm distance from the GC (1525 nm ± 14.7 nm). Further than 200 µm afar from the GC, the length increased exponentially to a mean length of 5.5 µm (at 250 µm: 5476 nm ± 179.6 nm), which corresponds to around 27 consecutive spectrin tetramers (**Figure 16, b**).

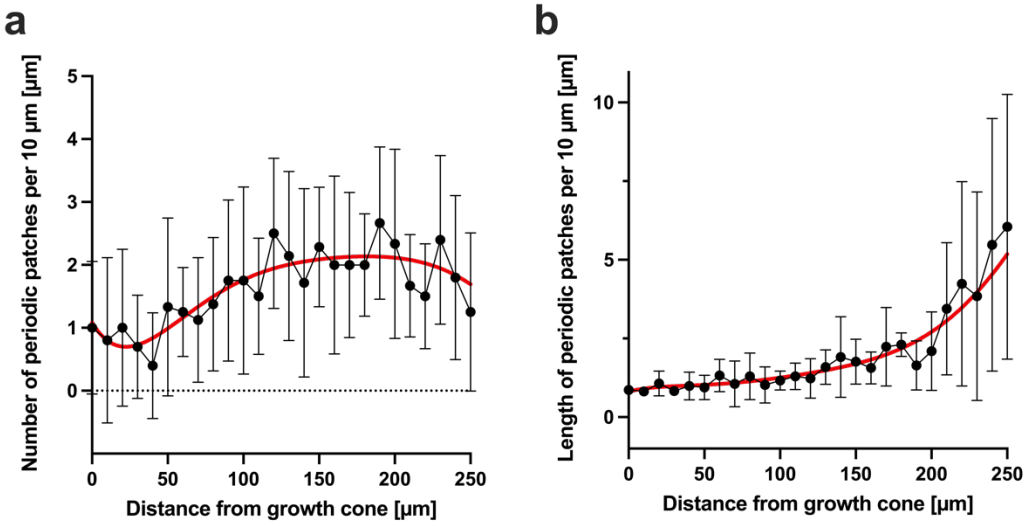

Figure 16: Quantification of periodic patch number and length along the axon. Cells were fixed on DIV 11, axons were stained for spectrin, and were imaged along the axon using STED microscopy. The number of periodic patches **(a)** increased, then decreased beyond 200 µm. The periodic patch length increased towards soma **(b)**. Data is displayed as mean ± SD. Sixth-order polynomial estimated curve fits are indicated by red lines. A total of 10 axons and at least 5 biological replicates, were examined. Not all axons could be included at distal points due to difficulties in tracking them back for long distances.

The average spacing of spectrin tetramers along the axon was measured to quantify any changes along the axon. Therefore, the distance of periodic spectrin signal peaks was measured using line intensity scans along periodic patches at different distances from the GC. Tetramer spacing slowly increased from around 190 nm between two spectrin signals close to the GC-base to 200 nm at 200 µm from the GC (10 µm: 191.2 nm ± 8.5 nm, 100 µm: 196.2 nm ± 9.9 nm, 200 µm from the GC: 204.2 nm ± 6.2 nm, as **Figure 17** shows).

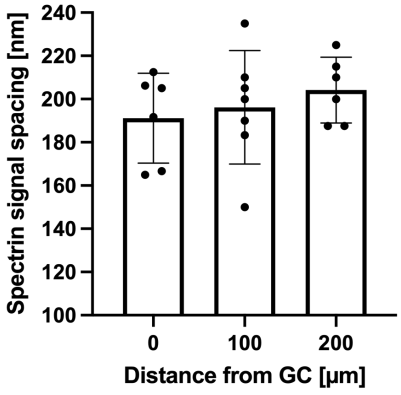

Figure 17: Development of the periodic spacing of spectrin tetramers along the axon. Cells were fixed on DIV 11, axons were stained for spectrin, and were imaged using STED microscopy. Three different, 10 µm long axonal segments were analyzed per axon, 0 µm, 100 µm, and 200 µm away from the growth cone. The average spacing slowly increased with increasing distance from the GC. Bars display mean ± SEM, at least 5 biological replicates were analyzed, and 11 axons were analyzed in total.

According to the findings so far, the development of the MPS in an outgrowing axon can be divided into three phases: an *assembly phase* during which multilocular periodic spectrin patches emerge along the axon, an *elongation phase* during which the number of patches increases and individual patches enlarge, and a final *coalescence phase* during which periodic patches coalesce and the MPS is closed (**Figure 18**).

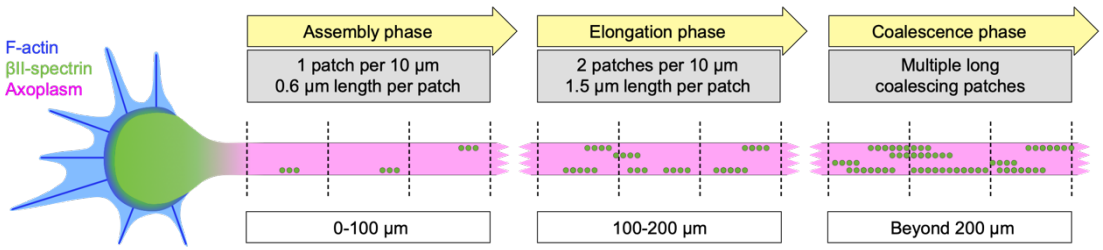

Figure 18: Development of the MPS in growing axons. Graphical illustration of the phases of MPS development along a growing axon. The dotted lines indicate 10 µm intervals along the axon. The growth cone is positioned on the left. Periodic patches are formed by periodic arrangements of βII-spectrin molecules (symbolized by green dots) close to the growth cone, the *assembly phase*. During the *elongation phase,* the number of patches increases and individual patches enlarge. These patches then coalesce during maturation and form the mature MPS, the *coalescence phase*.

3.1.2.3 Axonal diameter and spectrin periodicity behave opposite in the youngest axonal segment

Previous research has described the role of the MPS in regulating axonal diameter (Leite et al. 2016; Costa et al. 2020; Wang et al. 2020). To test a possible correlation, the axonal diameter along the developing axon was analyzed. As **Figure 19, b** shows, axonal diameter decreased approximately threefold over a distance of 250 µm from the GC (first 10 µm: 1.3 µm ± 0.2 µm, 250 µm from GC: 0.4 µm ± 0.1 µm). Therefore, the axonal diameter decreased while the spectrin periodicity increased (**Figure 14** and **Figure 19, a).** A correlation analysis of the two results revealed that the axonal diameter negatively correlates with spectrin periodicity with a Pearson coefficient r of -0.863 (**Figure 19, c**).

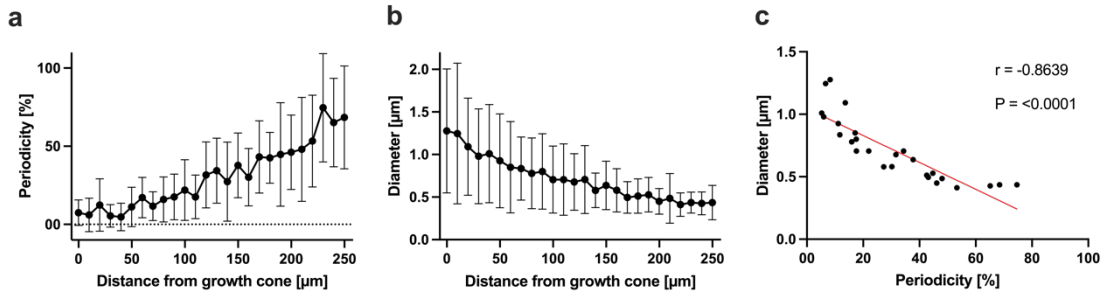

Figure 19: Increase of periodicity and reduction of axonal diameter along the axon. Cells were fixed on DIV 11, axons were stained for spectrin and tubulin, and were imaged using STED microscopy. **(a)**: Increase of periodicity along the growing axon (see **Figure 14**). **(b)**: Reduction in axonal diameter along the length of the axon, beginning at the growth cone base, in contrast to **(a)**. **(c)**: Correlation of **(a)** and **(b)** with simple linear regression marked red (Y = -0.1076*X + 1.045). Data is displayed as mean ± SD. At least 5 biological replicates were analyzed, and 11 axons were analyzed in total. Not all axons could be included at distal points due to difficulties in tracking them back for long distances.

3.2 Axonal regeneration

3.2.1 Reorganization of the MPS in axonal regeneration

3.2.1.1 Axonal regeneration in microfluidic chambers

To study the role of the axonal cytoskeleton during axonal regeneration, an axotomy was performed at DIV 11 in the MFCs using a cell culture pump (see 2.2.2.8). In a preliminary experiment, the time point of the first sights of regeneration was investigated. Therefore, using a fluorescence microscope at 20x magnification, MFCs were imaged before axotomy and then 5, 10, 15, 30, 60, 90, 120, 180, 240, 300, and 360 min and 24, 48, and 72 h after axotomy (data not shown). Regenerating axons were sighted first at 120 min after axotomy, and cultures died after DIV 13, which resembles 48 h after axotomy. A time span of 2 up to 24 h after axotomy was chosen to study the axonal cytoskeleton.

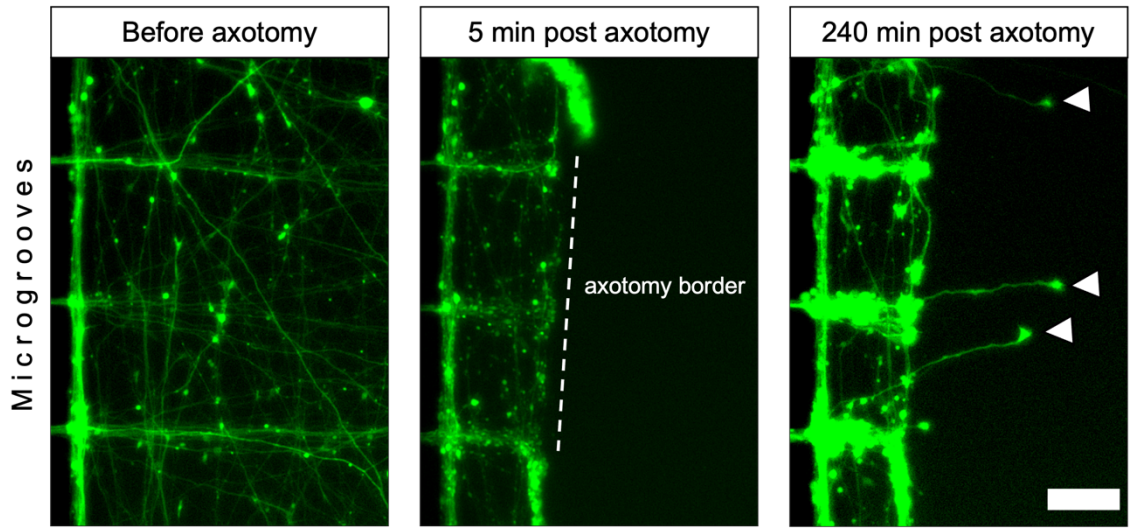

Figure 20: Representative image of axonal regeneration after an axotomy. Experiments were performed at DIV 11, using a conventional inverted fluorescence microscope at 20x magnification. In the representative images, axons were imaged right before, 5 min after, 240 min after the axotomy, and right before fixation. Microgrooves can be seen to the left of each image. Unlesioned axons can be seen before axotomy; the axotomy border can be seen in the second image. At 240 min after the axotomy, three regenerating axons with GCs can be seen, marked by white arrowheads. The scale bar is 30 μm.

To ensure STED imaging of regenerating axons only, that axons are cut sufficiently, and to identify if unlesioned axons cross the microgrooves, a novel method was developed. Therefore, corresponding images of the same region of the axonal compartment were taken right before, 5 min after, and 2, 3, 4, 5, 6, or 24 h, after the axotomy, right before fixation, using a conventional epifluorescence microscope. These images were aligned and compared. Regenerating axons were identified and marked (**Figure 20**, for a detailed explanation, see section 2.2.4.2). STED images were taken of the previously identified regenerating axons only, allowing to match live-cell microscopy with STED microscopy.

Axons were imaged from the GC towards the axotomy border; thus, the whole regenerating axonal segment was captured. An exception was made for axons of the 24-hour time point because axons were too long to be followed back to the axotomy border. Parameters regarding the development of periodicity and morphological aspects were investigated along the axon and its GC. A few distinctions had to be made for the comparison of regenerating and non-axotomized axons. Because the regenerating part of the cut axons was relatively short at 2 h after axotomy (**Figure 21**), only the first 10 μm of axons were compared to non-axotomized axons at all time points. This allowed for an in-depth analysis of cytoskeletal and morphological changes in the youngest part of the axon throughout the first 2 – 24 h after the axotomy.

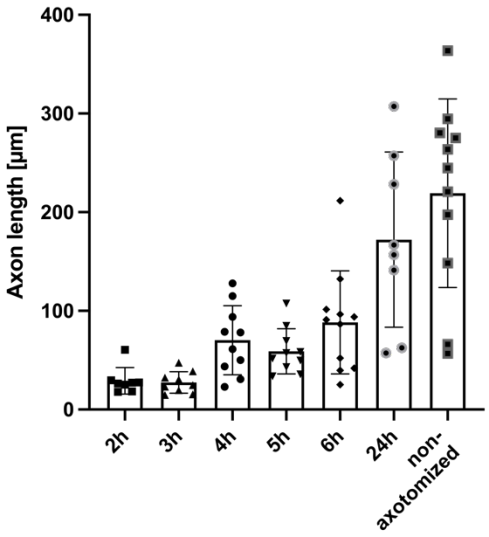

Figure 21: Length of analyzed regenerating axonal segments. Cells were fixed on DIV 11 at different time points after the axotomy or non-axotomized. Axons were stained for spectrin and imaged using STED microscopy. Graphical display of the length of regenerating segments at different time points used for analysis, assessed by STED microscopy. The overall trend is an increasing outgrowth length after axotomy. The 24-hour time point does not show the actual length of the regenerating segment due to the immense length of these segments after 24 h. Non-axotomized axons were captured for a distance of 200 µm or longer, if possible. The bars represent mean ± SD. The number of biological replicates was 3, for each condition, at least 8 axons were examined, and 67 axons were analyzed in total.

3.2.1.2 Spectrin periodicity and number of periodic patches are increased early after axotomy

As can be seen in the first set of experiments, the MPS developed in non-axotomized axons in a proximal to distal manner with periodic patches that form and coalesce in three distinct phases. To investigate the role of the MPS in axonal regeneration, the development of the MPS was evaluated in regenerating axons at different time points after axotomy and was compared to non-axotomized axons.

Surprisingly, the first 10 µm of regenerating axon adjacent to the GC showed higher percentages of periodicity at 2 h after axotomy, compared to non-axotomized axons, as shown in **Figure 22, a**. This development in regenerating axons happened much quicker than in non-axotomized axons, as spectrin periodicity was almost 3.5-fold higher compared to non-axotomized axons (2 h: 25.7% ± 7.3% vs. non-axotomized: 7.5% ± 2.4%). It is interesting to note that the periodicity of regenerating axons of later time points was more similar to that of the non-axotomized axons.

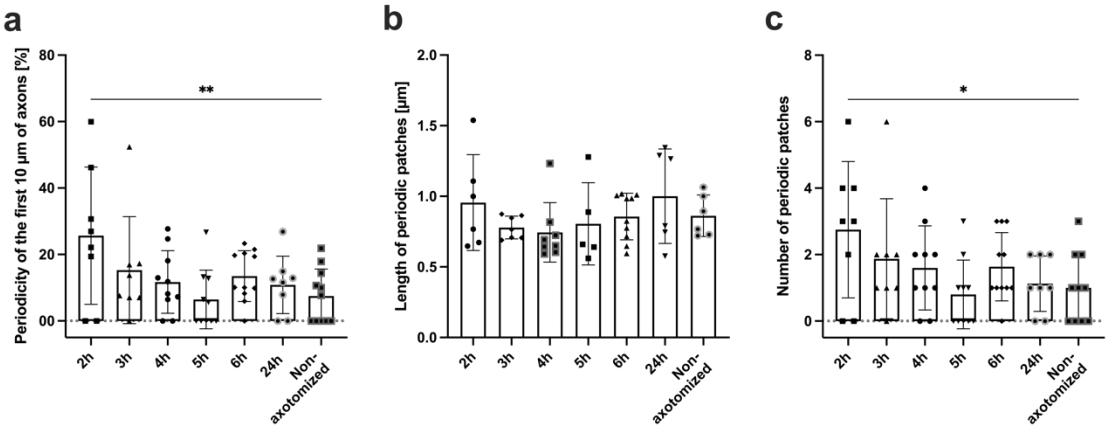

Figure 22: Comparison of MPS development of regenerating axons and non-axotomized axons. Cells were fixed on DIV 11 at different time points after the axotomy or non-axotomized. The axons were stained for spectrin and imaged using STED microscopy. **(a)**: Comparison of spectrin periodicity of regenerating axons at different time points and non-axotomized axons. At the 2-hour time point axons displayed significantly more periodicity when compared to non-axotomized axons. **(b)**: Comparison of length of periodic patches of regenerating axons at different time points and non-axotomized axons. There were no significant changes detected. **(c)**: Comparison of the number of periodic patches of regenerating axons at different time points and non-axotomized axons. The 2-hour time point displays significantly more periodic patches compared to non-axotomized axons. **(a-c)**: The first 10 µm of the axon adjacent to the GC were analyzed. Bars represent mean ± SD and groups were compared using one-way ANOVA, followed by Dunnett's multiple comparisons test. A minimum of 8 axons were analyzed per condition, with a total of 67. The number of biological replicates was three.

The length of periodic patches did not change significantly over the examined time span, compared to non-axotomized axons (2 h: 0.96 µm ± 0.1 µm vs. non-axotomized: 0.86 µm ± 0.06 µm, **Figure 22, b**). However, as shown in **Figure 22, c**, compared to non-axotomized axons, the number of periodic patches was increased nearly threefold at 2 h after axotomy (2 h: 2.7 ± 0.7 vs. non-axotomized: 1.0 ± 0.3). The number of periodic patches quickly decreased at the later time points and displayed numbers comparable to non-axotomized axons.

These findings indicate that early after axotomy, regenerating axons transiently form more periodic spectrin patches in the outgrowing region of the axon. Compared to non-axotomized axons, this leads to a higher level of periodicity and a quicker assembly phase.

3.2.1.3 Regenerating axons are decreased in diameter

To assess the development of the axonal diameter during axonal regeneration, the axonal diameter of the axonal segment adjacent to the GC was measured at different time points after axotomy and compared to non-axotomized axons.

Overall, the axonal diameter of the first 10 µm of the axon was decreased in regenerating axons, compared to non-axotomized, but steadily increased over time (**Figure 23**). At the 2-hour time point, the axonal diameter was reduced almost threefold (2 h: 0.5 µm ± 0.1 µm vs. non-axotomized: 1.3 µm ± 0.2 µm). Up to 24 h after axotomy, the axonal diameter was

still significantly reduced by almost twofold (24 h: 0.7 µm ± 0.1 µm). The trends of decreasing spectrin periodicity and increasing axonal diameter over time suggest a correlation likewise to **Figure 19**, but note that contrariwise to the significant increase of periodicity at 2 h in **Figure 22, a**, the reduction of axonal diameter is significant in all time points after axotomy.

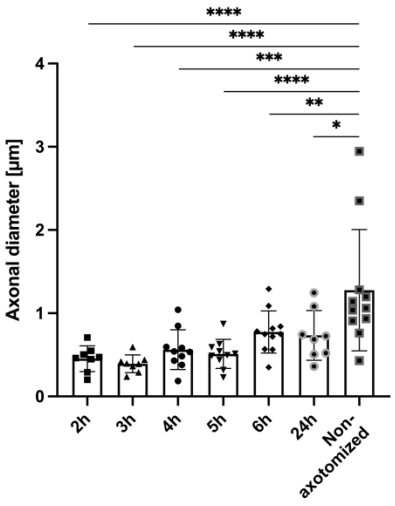

Figure 23: Development of axonal diameter during regeneration. Cells were fixed on DIV 11 at different time points after the axotomy or non-axotomized. Axons were stained for tubulin and imaged using STED microscopy. Analyzed were the first 10 µm of axons adjacent to the GC. The reduction of axonal diameter is significant at all time points compared to non-axotomized axons. The axonal diameter increases over time but is still significantly reduced at 24 h after axotomy. Note, that in **Figure 22, a**, only the 2-hour time point showed a significant increase in periodicity. Bars show mean ± SD and groups were compared using one-way ANOVA, followed by Dunnett's multiple comparisons test. A minimum of 8 axons were analyzed per condition, with a total of 67. The number of biological replicates was three.

3.2.1.4 Axonal outgrowth speed increases late after axotomy

To analyze whether the axonal outgrowth speed was faster after axotomy, the axonal outgrowth speed of non-axotomized and regenerating axons was measured. Therefore, 10-minute-long time-lapse videos at 20x magnification of axons of DIV 10 neurons were used (for details, see section 2.2.5.3). Although the cells were fixed on DIV 10, data was assumed to be representative for the standard experiment setup due to the same neuronal cells being used in the same culturing conditions in the MFCs.

As **Figure 24** shows, axonal outgrowth velocity was significantly increased 4 and 6 h after axotomy but not 2 h after axotomy, compared to non-axotomized (non-axotomized: 18.3 µm/h ± 2.3 µm/h, 2 h: 20.5 µm/h ± 2.1 µm/h, 4 h: 30.8 µm/h ± 3.0 µm/h, and 6 h after axotomy: 34.5 µm/h ± 2.7 µm/h).

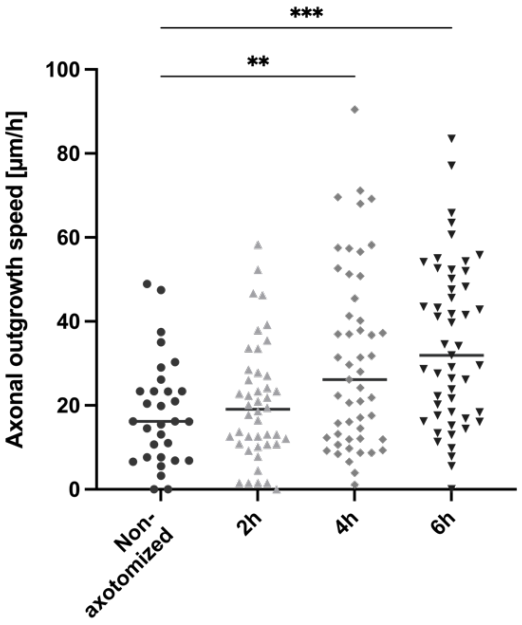

Figure 24: Comparison of axonal outgrowth speeds of non-axotomized and regenerating axons. Axonal outgrowth speed was measured using 10-minute-long time-lapse videos at 20x magnification of DIV 10 axons. Note, that axonal outgrowth speed is increased 4 and 6 h after axotomy, but not at 2 h, compared to non-axotomized. The line represents mean and groups were compared using one-way ANOVA, followed by Dunnett's multiple comparisons test. A minimum of 31 axons were analyzed per condition, with a total of 177. The number of biological replicates was three.

3.2.2 Morphological changes in axonal regeneration

3.2.2.1 GCs of regenerating axons were significantly smaller in area, length, and width but increased over time.

To investigate the effect of regeneration on the morphology of the newly formed GC, GC area, length, and width of regenerating axons at different time points after axotomy were measured and compared to non-axotomized GCs (see **Figure 25** for representative micrographs).

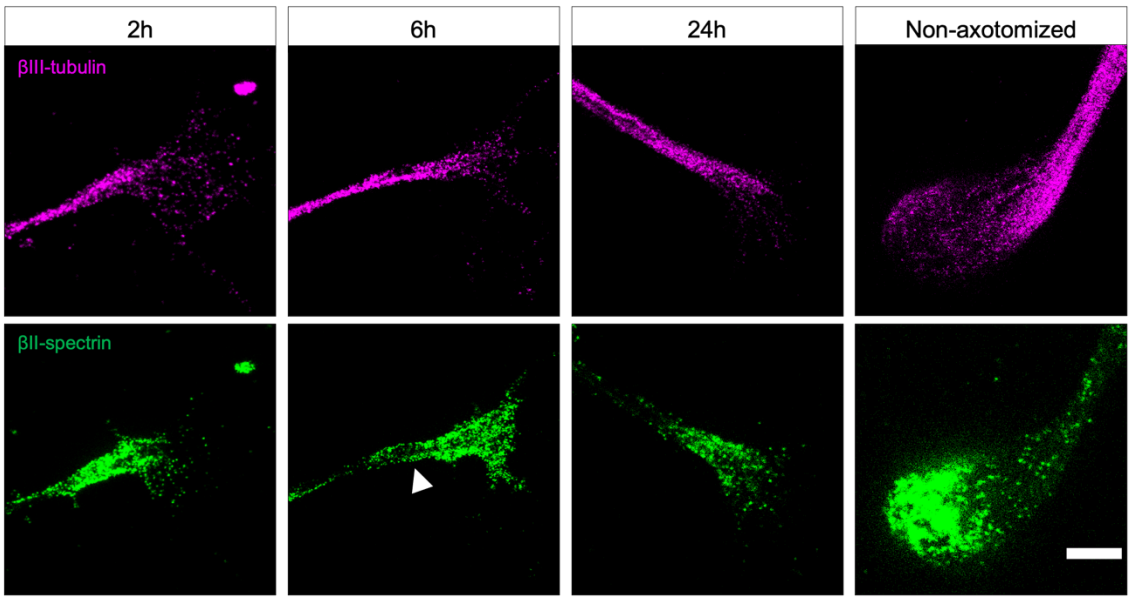

Figure 25: Representative images of GCs of regenerating axons and non-axotomized axons. Cells were fixed on DIV 11 at different time points after the axotomy or non-axotomized. The axons were stained for spectrin and tubulin and imaged using STED microscopy. Note the size difference between regenerating GCs and non-axotomized GCs. A white arrowhead indicates a spectrin neck (see 3.2.2.2). The scale bar is 2 µm.

As shown in **Figure 26, a**, the GC area was reduced significantly in all time points after axotomy. Remarkably, the GC area was reduced almost five-fold at 2 h after axotomy. Although the GC area increased twofold over 24 h of regeneration, it did not attain non-axotomized sizes in this timespan (2 h: 3.7 $\mu m^2 \pm 0.8 \mu m^2$, 24 h: 8.0 $\mu m^2 \pm 1.2 \mu m^2$, and non-axotomized axons: 20.5 $\mu m^2 \pm 1.9 \mu m^2$).

The length of regenerating GCs was decreased twofold at 2 h after axotomy, compared to non-axotomized axons, as **Figure 26, b** shows. Up to 6 h after axotomy, the GC length was still significantly reduced, but not at 24 h after axotomy (2 h: 3.6 µm ± 0.4 µm, 6 h: 5.0 µm ± 0.4 µm, 24 h after axotomy: 5.3 µm ± 0.7 µm, and non-axotomized axons: 7.4 µm ± 0.5 µm).

In contrast to non-axotomized axons, the width of regenerating GCs was reduced by nearly 2.5-times at the 2-hour time point, as **Figure 26, c** shows. Although the GC width increased over 24 h of regeneration, it did not reach non-axotomized sizes in this timespan. At 24 h after axotomy, GC width was still reduced by 1.8-times when compared to non-axotomized (2 h: 1.9 µm ± 0.3 µm, 24 h: 2.6 µm ± 0.4 µm, and non-axotomized axons: 4.6 µm ± 0.5 µm).

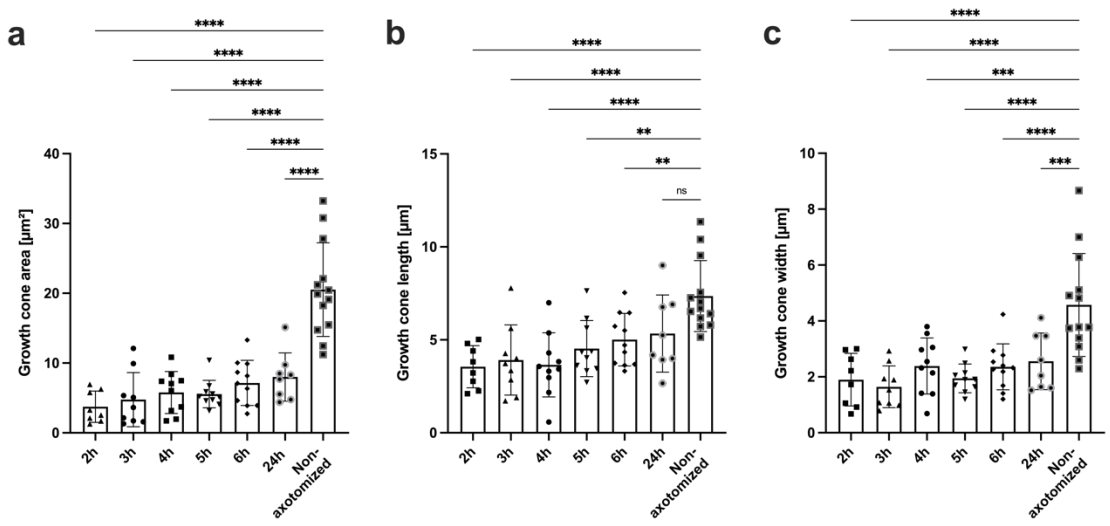

Figure 26: Development of axonal GC area, length, and width over time. Cells were fixed on DIV 11 at different time points after the axotomy or non-axotomized, axons were stained for spectrin, and imaged using STED microscopy. GC area **(a)**, length **(b)**, and width **(c)** are significantly decreased after axotomy, compared to non-axotomized axons, except for the GC length 24 h after axotomy. GC area, length, and width increased over time but did not reach non-axotomized values over the examined timespan. Bars represent mean ± SD and groups were compared using one-way ANOVA, followed up by Dunnett's multiple comparisons test. For each condition, at least 8 axons were examined, the number of biological replicates was 3, and 67 axons were analyzed in total.

3.2.2.2 Distribution of spectrin and tubulin along the GC and axon of regenerating axons

For the next experiment, line intensity scans along the GC and axon were carried out, similarly to the non-axotomized axons, to see if regenerating GCs also exhibit an enrichment of spectrin. In order to compare the several time points after the axotomy, the intensity along the length of the GC was averaged and compared to the intensity along the first 10 m of the axon adjacent to the GC, as can be seen **Figure 27**.

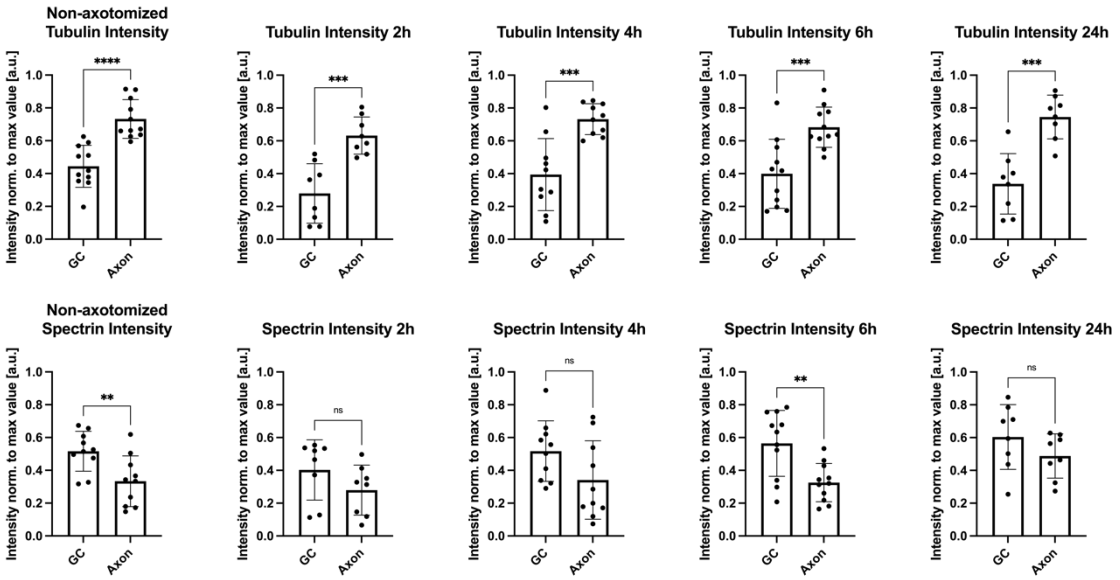

Figure 27: Distribution of spectrin and tubulin along regenerating axons and growth cones. Cells were fixed on DIV 11 at different time points after the axotomy or non-axotomized, axons were stained for spectrin, and imaged using STED microscopy. Line intensity scans along the axons of sampled groups at various time intervals after and before axotomy were evaluated. Lines included the whole growth cone and the first 10 µm of the axon. The individual maximum intensity was used to standardize the intensity measurements, which were averaged for every 1 µm. While the tubulin signal is weaker in the GC in all groups as compared to the axon, the spectrin signal intensity peaks at the growth cone at 6 h after axotomy and in non-axotomized axons. Groups were compared using unpaired t tests. Data is shown as mean ± SD. A total of 47 axons from at least 4 biological replicates were examined.

As was the case for the non-axotomized axons, tubulin intensity decreased in the GC at all time points following axotomy, most likely as a result of microtubule splay (see **Figure 8** and **Figure 9**). Even though a trend could be inferred, it is interesting to note that, except for the 6-hour time point, the enrichment of spectrin within the GC did not persist in regenerating GCs (Spectrin: non-axotomized axons: GC 0.51 vs. axon 0.33, 2 h: GC 0.4 vs. axon 0.28, 4 h: GC 0.52 vs. axon 0.34, 6 h: GC 0.56 vs. axon 0.33, 24 h: GC 0.6 vs. axon 0.49).

3.2.2.3 A fraction of regenerating axons showed an enrichment of spectrin in the region proximal to the GC

Some of the regenerating axons showed an accumulation of spectrin at the GC neck, which will be referred to as "spectrin neck" (for example, see white arrowhead in **Figure 25**). A spectrin neck was defined as an increase in spectrin signal in comparison to the more proximal axon, at the axonal segment directly connected to the GC, that was at least 600 nm long and no greater than 3 µm in length. The intensity rise had to exceed the 75th percentile of the measured 4 µm, and the intensity values in the first micrometer had to be 1.5 times higher than those in the second to fourth micrometer. Averaged over all time points, a fraction of 37% (36.9% ± 5.1%) of regenerating axons displayed spectrin necks, whereas non-axotomized axons displayed none, as can be seen in **Figure 28**.

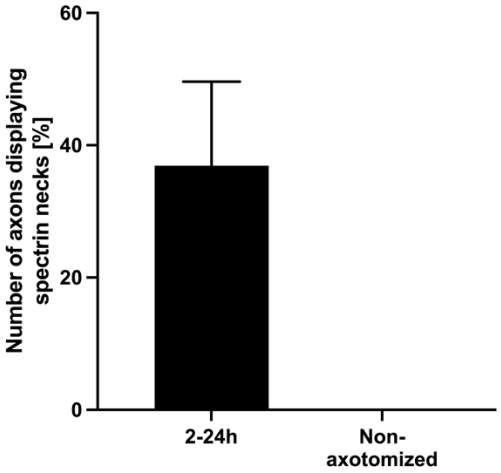

Figure 28: Comparison of regenerating and non-axotomized axons displaying spectrin necks. Cells were fixed on DIV 11 at different time points after the axotomy or non-axotomized, axons were stained for spectrin, and imaged using STED microscopy. Spectrin necks were not displayed by non-axotomized axons, whereas regenerating axons displayed a variating percentage of axons with spectrin necks but with no overall trend. The bar represents mean ± SD. For each condition, at least 8 axons were examined, the number of biological replicates was 3, and 67 axons were analyzed in total.

Line intensity scans were performed along the first 4 µm of axon close to the GC to visualize the presence of spectrin necks. Axon data with and without spectrin necks were compared. As can be seen in **Figure 29**, axons with spectrin necks showed a visible increase in spectrin intensity close to the GC.

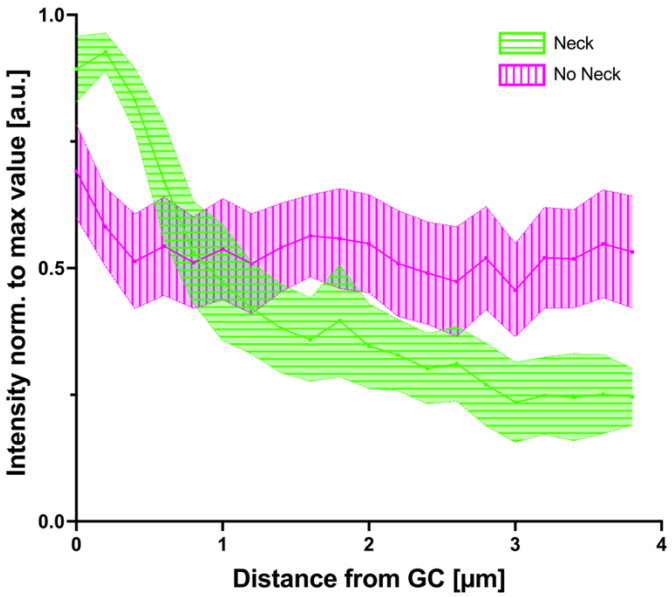

Figure 29: Comparison of spectrin intensity distribution in axons with or without spectrin neck. Cells were fixed on DIV 11 at different time points after the axotomy or non-axotomized, axons were stained for spectrin, and imaged using STED microscopy. The first 4 µm of the axon next to the GC were examined using line intensity scans. In this graph, all time points following axotomy are merged. For the definition of spectrin neck, see section 3.2.2.3. Data is shown as mean ± 95% confidence interval. For each condition, at least 21 axons were examined, with a total of 56 axons. Three biological replicates were examined.

In summary, these results show that regenerating axons transiently exhibit a higher degree of spectrin periodicity, due to an increased periodic spectrin patch density, compared to non-axotomized axons. Regenerating axons also displayed a constant smaller axon diameter and a decreased growth cone size. The axonal outgrowth speed was increased at 4 and 6 h after axotomy. Furthermore, a significant fraction of regenerated axons displayed spectrin accumulation at the GC neck.

3.3 Effect of calpain inhibition on regenerating axons

3.3.1 Effects on the axonal cytoskeleton

3.3.1.1 Experimental setup

The previous set of experiments showed that spectrin periodicity was increased early after axotomy. The third set of experiments aimed to assess whether inhibition of the spectrin-cleaving enzyme calpain would be beneficial for axonal regeneration and outgrowth or not. Therefore, axons were treated with 10 µM of the calpain inhibitor calpeptin dissolved in DMSO or DMSO alone as a control. Axons were incubated for 1 h before axotomy and then fixed 120 min after the axotomy (see **Figure 30**). Calpeptin or DMSO were administered only into the axonal compartment of the MFC.

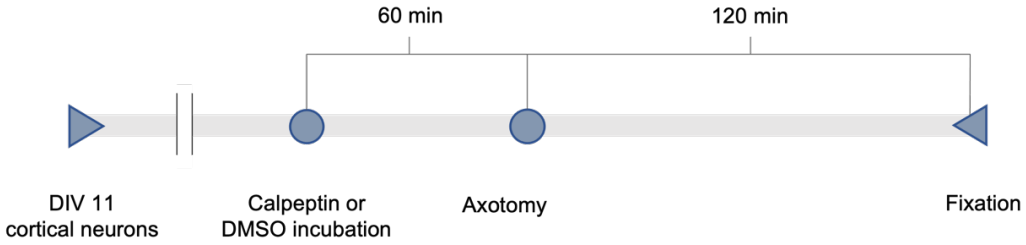

Figure 30: Experimental procedures for treatment of axons with calpeptin or DMSO. Experiments were carried out on DIV 11 of cultured neurons. At 1 h before the axotomy, axons were incubated with calpeptin or DMSO. Axotomy was performed and cells were fixed 120 min after the axotomy. Axons were then stained for spectrin and imaged using STED microscopy.

After identification of regenerating axons (see 2.2.4.2 and **Figure 20**), spectrin periodicity and periodic patches of the first 10 µm of axon adjacent to the GC were captured using STED microscopy and then analyzed (see **Figure 31**).

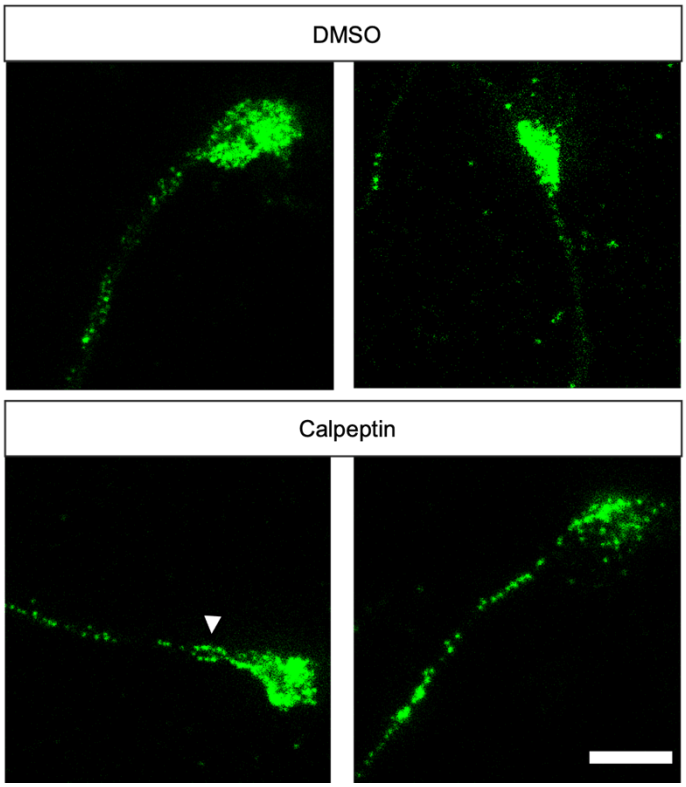

Figure 31: Representative images of regenerating axons incubated with calpeptin or DMSO. Cells were fixed on DIV 11, 120 min after the axotomy, axons were stained for spectrin, and imaged using STED microscopy. Note the periodic patches in calpeptin-treated axons. A spectrin neck is marked by a white arrowhead. The scale bar is 2 μm.

3.3.1.2 Effect on the MPS

Treatment of axons with calpeptin did indeed have an effect on the MPS, as the periodicity of treated axons was increased more than three times in the first 10 μm of the axon at 2 h after axotomy, compared to the control group (Calpeptin: 36.6% ± 9.6% vs. DMSO: 12.7% ± 3.4%, see **Figure 32, a**).

As can be seen in **Figure 32, b**, the number of periodic patches at 2 h after axotomy in the first 10 μm of axon did not significantly differ between the two groups (Calpeptin: 1.9 ± 0.4 vs. DMSO: 1.5 ± 0.4) However, as **Figure 32, c** shows, the length of periodic patches at 2 h after axotomy in the first 10 μm of the axon was increased almost 2.5-fold in calpeptin-treated neurons, compared to control group (Calpeptin: 1.6 μm ± 0.4 μm vs. DMSO: 0.7 μm ± 0.2 μm)

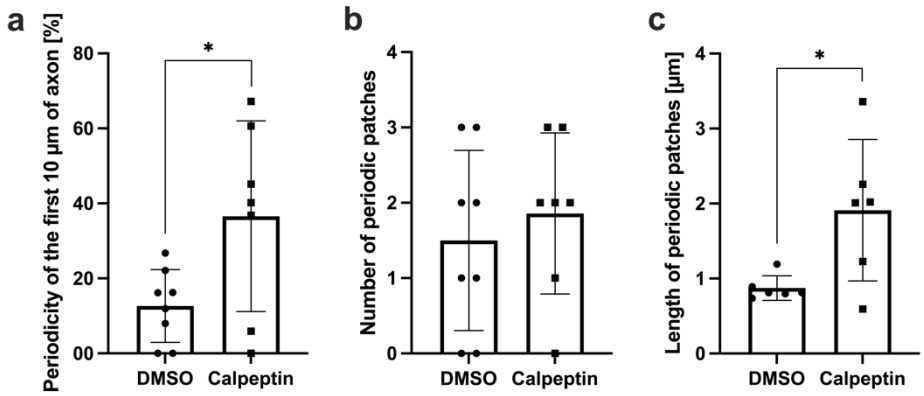

Figure 32: Comparison of periodicity parameters between calpeptin or DMSO-treated axons. The cells were fixed on DIV 11, 120 min after the axotomy, axons were stained for spectrin, and imaged using STED microscopy. The first 10 µm of axon close to the GC were examined. Calpeptin-treated axons (10 µM) showed an increased periodicity, as well as an increased length of periodic patches, compared to the DMSO control group **(a, c)**. The number of periodic patches, however, did not change between both groups **(b)**. Bars represent mean ± SD and groups were compared using unpaired t test **(a, b)** or Kolmogorov-Smirnov test (as data was not normally distributed) **(c)**. For each condition, at least 7 axons were examined in 3 biological replicates, with a total of 15 axons.

3.3.1.3 Distribution of spectrin necks

To test whether inhibition of calpain using calpeptin affected the presence of spectrin necks, STED images of the GC base were analyzed. Interestingly, axons treated with calpeptin displayed spectrin necks slightly more often than those treated with DMSO, although not significantly (Calpeptin: 33.3% vs. DMSO: 16.7%), as shown in **Figure 33**.

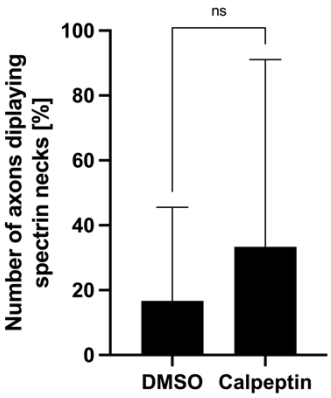

Figure 33: Effect of calpeptin on the number of axons displaying spectrin necks. Cells were fixed on DIV 11, 120 min after the axotomy, axons were stained for spectrin, and imaged using STED microscopy. Analyzed were the first 10 µm of axon adjacent to the GC. Calpeptin-treated axons displayed spectrin necks slightly more often than the DMSO control group. For the definition of spectrin neck, see section 3.2.2.3. For each condition, at least 7 axons were examined in 3 biological replicates, with a total of 15 axons. There was no significant difference detected according to unpaired t test with Welch's correction.

3.3.1.4 Distribution of spectrin in regenerating axons treated with calpeptin

In a manner similar to the investigations in section 3.2.2.2, line intensity scans were used to examine the effect of calpeptin on the distribution of spectrin along the GC and the distal axon, as can be seen in **Figure 34**.

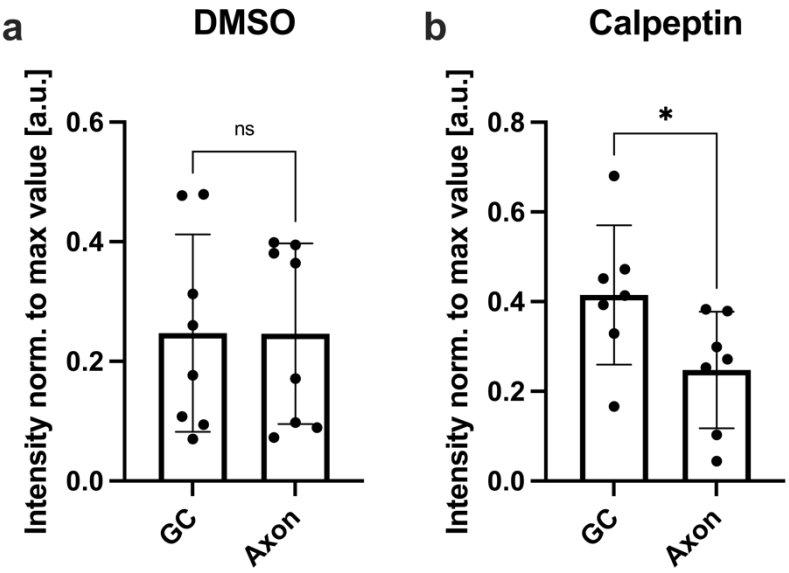

Figure 34: Distribution of spectrin in axons treated with DMSO or calpeptin. Quantitative analysis of line intensity scans of axons of sampled groups given DMSO or calpeptin. Cells were fixed on DIV 11, 120 min after the axotomy, axons were stained for spectrin, and imaged using STED microscopy. Line scans were drawn from the growth cone tip along the GC and the first 10 µm of the axon. No distinction in spectrin intensity between GC and axon was found in axons treated with DMSO **(a)**. Compared to the axon, spectrin-fluorescence intensity peaks in the growth cone of axons treated with calpeptin **(b)**. The data is shown as mean ± SD and unpaired t tests were used to compare two groups. For each condition, at least 7 axons were examined in 3 biological replicates, with a total of 15 axons.

It is interesting to note that calpeptin-treated axons at 2 h after axotomy demonstrated a considerable enrichment of spectrin inside the GC, while neither the DMSO-treated group nor the untreated group from the prior experiment did at the same time point (Calpeptin: GC 0.41 vs. axon 0.25, DMSO: GC 0.25 vs. axon 0.25).

3.3.2 Effects on axonal outgrowth

After identifying calpain inhibition as having an effect on the MPS, the effect of calpeptin on the axonal outgrowth was studied next. Therefore, overview images at 20x magnification for identification of regenerating axons were re-evaluated (see 2.2.4.2 and **Figure 20**). The number of regenerating axons per 9 microgrooves (in general, 9 microgrooves were in view at 20x magnification) was counted, and the outgrowth length of regenerating axons was measured.

As **Figure 35, a** shows, the regenerating axonal segments were slightly longer in calpeptin-treated axons, but not significantly, compared to the control group (Calpeptin: 21.4 µm ±

1.8 μm vs. DMSO: 18.1 μm vs. 2.8 μm). The number of regenerating axons, however, was significantly increased in analyzed images of calpeptin-treated chambers, in contrast to the control group (Calpeptin: 3.2 ± 0.6 vs. DMSO: 1.4 ± 0.4), as can be seen in **Figure 35, b**.

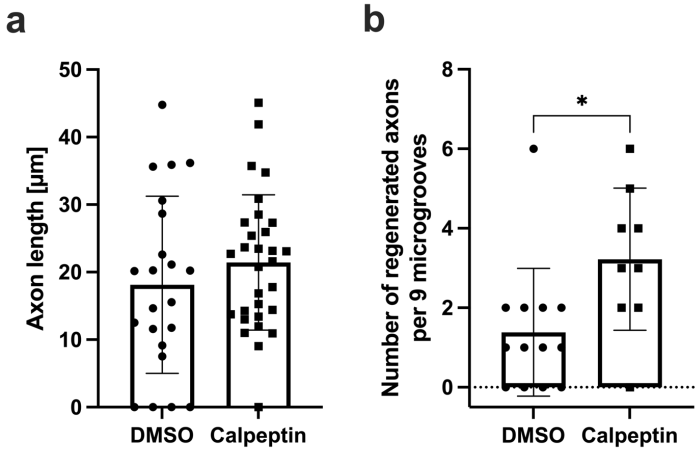

Figure 35: Effects of calpeptin on axonal outgrowth and regeneration. Cells were imaged on DIV 11, 120 min after the axotomy, at 20x magnification, using a conventional inverted fluorescence microscope. Axons are treated with 10 μM of calpeptin or an equal amount of DMSO. Bars represent mean ± SD and groups were compared using non-parametric Mann-Whitney U test. **(a)**: Axon length did not differ significantly between calpeptin or DMSO-treated groups. For each condition, at least 22 axons were examined in 3 biological replicates, with a total of 52 axons. **(b)**: In comparison to the DMSO control group, the number of regenerated axons per 9 microgrooves was significantly greater in the chambers treated with calpeptin. For each condition, at least 22 axons were examined in 3 biological replicates, with a total of 52 axons.

4 Discussion

4.1 Introduction

To investigate the formation and development of the axonal MPS in outgrowing and regenerating axons, primary embryonic cortical neurons of the rat were cultured in MFCs to allow the isolated evaluation of axons using STED microscopy. As revealed by the nanoscale analysis of STED microscopy, growing axons exhibit a distinct spatial and temporal increase of spectrin periodicity. This increase happens in a gradient from the distal growth cone towards the soma. The building blocks of MPS formation are periodic arrangements of βII-spectrin tetramers, the periodic patches. These periodic patches increase in number and size along the growing axon and eventually coalesce, forming the mature MPS. The MPS transiently develops more distally and more quickly in regenerating axons than in non-axotomized axons. This study also identified calpeptin as a promising drug for increasing periodicity early after axotomy of the MPS, which could lead to enhanced axonal regeneration.

4.2 Distribution of tubulin, spectrin, and F-actin along the axon and its GC

Previous studies found an enrichment of spectrin in the axonal GC (Levine and Willard 1981; Matsuoka et al. 2000; Galiano et al. 2012; Tian et al. 2012). This present study further underlines the role of spectrin in the GC, as the enrichment of spectrin was present in non-axotomized GC and at least as a trend in regenerating GCs at different time points after axotomy. This study also characterized the level of enrichment along the axon and GC, as spectrin was especially enriched in the center of the GC, close to the F-actin arc on top of the GC.

Enrichment of spectrin inside the GC could resemble a pool of vesicles that were transported to the GC, as spectrin is also an important protein for linking vesicles to microtubule motor proteins, allowing axonal transport (Holleran et al. 1996; Takeda et al. 2000). Spectrin was also first described as an unknown protein transported along axons (Levine and Willard 1981).

The enrichment of spectrin inside the GC could also resemble a reservoir of spectrin tetramers, waiting to be incorporated into the axonal MPS, as the GC is always on top of the growing axon.

Spectrin enrichment inside the GC could also point to its role as a binding partner of actin and membrane proteins like ankyrin-B. Therefore, spectrin tetramers could work as a lattice or mesh inside the GC, stabilizing it or supporting the motility of the GC. The use of 2D autocorrelation analysis could further evaluate a lattice-like distribution of spectrin in the GC,

as it has been shown for βIII-spectrin in the somatodendritic region of some neurons (Han et al. 2017). Interestingly, in co-stainings of spectrin and F-actin, spectrin was also often accumulated in proximity to the base of F-actin filopodia. This could be due to an interaction of actin and spectrin during protrusion and retraction of the filopodia of the GC or a role for spectrin as an anchor for F-actin. The cellular interplay of spectrin and actin in cell motility has been described before (Ghisleni et al. 2020) but has not been shown inside the axonal GC. The results of this present study suggest a likewise interaction, but live-cell microscopy is needed to elucidate this possible connection further.

4.3 Spatial and temporal development of the MPS along the axon

Previous studies described the development of the axonal MPS to be in a proximal to distal pattern (Zhong et al. 2014; Han et al. 2017; Lorenzo et al. 2019). It was also stated that the MPS covers the whole axonal shaft at DIV 9 in hippocampal rat neurons (Zhong et al. 2014). This study confirms these findings partly, as the axonal MPS did extend in a proximal to distal pattern. It can be further specified that growing axons exhibit a distinct spatial and temporal increase of spectrin periodicity. This increase happens in a gradient from the distal growth cone towards the soma. Also, in contrast to previous work, the MPS did not cover the whole axonal shaft on DIV 11, as the youngest part of the axons did not show periodicity. The timespan of MPS development for a newly outgrown axonal segment was characterized to be around 14 h in the present culture conditions. Therefore, it can be assumed that it is not the normal state that growing axons exhibit MPS throughout the axonal shaft after a certain time in culture. Instead, the newly outgrown part of the axon forms without displaying MPS and then develops its MPS during maturation.

This also illustrates that the MPS is not primarily necessary for the outgrowth of axons but rather facilitates other functions, like stabilization of the axon (Hammarlund et al. 2007; Dubey et al. 2020), electrical conductivity (Costa et al. 2020), the control of axonal diameter (Leite et al. 2016; Costa et al. 2020; Wang et al. 2020), axonal transport of cargoes (Wang et al. 2020), and the lattice-like organization of proteins into the axon (Xu et al. 2013; Vassilopoulos et al. 2019; Zhou et al. 2019; Li et al. 2020). This study, therefore, further confirms the development of the MPS in a proximal to distal pattern and characterizes the spatial and temporal dimensions of MPS development along the youngest part of the axon.

4.4 Periodic patches are the building blocks of MPS formation

So far, the exact sequence of MPS assembly along the growing axon has not been reported. As this study shows, the MPS does not simply progress continuously along the axon following the GC. Like building blocks, the MPS is formed on the nanoscale by the assembly of multiple periodic patches along the growing axon, consisting of spectrin tetramers. This can be described in three phases: an *assembly phase*, an *elongation phase*, and finally, a *coalescence*

phase. In the *assembly phase*, periodic patches are assembled in the axonal segment close to the GC, at a frequency of around 1 patch per 10 μm. The periodic patches then double in number and elongate over a time span of around 11 h, the *elongation phase*. During the *coalescence phase*, periodic patches finally coalesce and form the mature MPS. This formation happens in a spatial and temporal gradient from the GC base towards the more proximal regions of the axon.

The results obtained in this study could suggest the GC or its neck as a potential assembly site for periodic patches for three reasons. Firstly, the GC and its neck sit on the very top of the growing part of the axon, the segment where the new MPS needs to be formed. Secondly, periodic patches were routinely seen very close to the GC. Thirdly, because spectrin is greatly abundant in the GC, it may serve as a reservoir for the incorporation of spectrin tetramers into the developing axon.

The formation of the MPS through periodic spectrin patches suggests the existence of assembly factors, molecules, that start the formation of periodic patches. So far, much is known about the structure of the MPS and its functions, but little about the molecular background of its formation. A recent study evaluated further binding partners for actin and spectrin, using co-immunoprecipitation and mass spectrometry (Zhou et al. 2022). The identified binding partners included different cytoskeletal proteins, transmembrane proteins, and sub-membranous signaling molecules. Interaction analyses and knockout studies could elucidate their role in the assembly of periodic patches and the formation of the MPS.

It is noteworthy that the number of periodic patches not only increased close to the GC but also at distances of 100 – 200 μm away from the GC. A possible explanation could be assembly molecules that are integrated into the axon close to the GC and then stay on the way as the axon continues to outgrow. As demonstrated previously, the prevalence of MPS in dendrites depends to some extent on local spectrin concentrations and the presence of ankyrin-B (Zhong et al. 2014). As shown in the current study and by others, spectrin and ankyrin-B (Galiano et al. 2012) are, in fact, highly enriched in the GC. Surprisingly, despite high concentrations of spectrin in the GC, periodicity or periodic patches were never detected inside the GC in our sample size. This result might be explained by the absence of assembly factors inside the GC, which could be restricted to axons and present only in the GC's neck.

Although a relatively small sample size and the need for automated quantification, these results provide evidence on the nanoscale that periodic patches are indeed the building blocks of MPS formation. This study also highlights the role of the GC and its neck in the formation and development of the axonal MPS.

4.5 Role of the MPS in regulation of the axonal diameter

The role of the MPS in the regulation of the axonal diameter has been discussed before (Leite et al. 2016; Costa et al. 2020; Wang et al. 2020). The current study shows that the decreasing axonal diameter negatively correlates with the increasing development of the MPS. Therefore, the youngest part of the axon shows the greatest axonal diameter. This lends support to the notion of progressive axonal constriction throughout MPS formation and maturation along the axon (Leite et al. 2016). Interestingly, destabilization of the MPS using trophic factor withdrawal did not lead to a reduction of axonal diameter (Unsain et al. 2018). A role for the periodically distributed actin capping protein adducin in the regulation of axonal diameter has been discussed (Leite et al. 2016). Whether the observed reduction of axonal diameter is caused by the implementation of adducin into the newly forming MPS (Leite et al. 2016) or the presence of NMII-molecules inside the axon (Vassilopoulos et al. 2019; Costa et al. 2020; Wang et al. 2020) remains unclear. Co-stainings of the implementation of spectrin, F-actin, adducin, and NMII along the axon could, therefore, provide further insight.

4.6 Spectrin periodicity is transiently increased early in axonal regeneration

Several reports have discussed the role of the MPS in axonal degeneration (Unsain et al. 2018; Wang et al. 2019). So far, the role of the MPS in axonal regeneration has not been investigated. This study provides an analysis of the temporal changes in the MPS development in the outgrowing regenerating axon in an *in-vitro* lesion approach. Regenerating axons show a transient increase in periodicity and in the number of periodic patches at an early time point after the axotomy. This is especially interesting, as MPS degeneration preceded axonal fragmentation in axons that were axotomized or withdrawn of trophic factors (Unsain et al. 2018; Wang et al. 2019). The transient increase in periodicity could be explained by increased levels of free spectrin after the axotomy, as overexpression of spectrin increased the abundance of MPS in dendrites (Zhong et al. 2014). Additionally, the inhibition of the spectrin-cleaving enzyme calpain using calpeptin increased periodicity even more shortly after axotomy in the current study. Another possible explanation could be the transient upregulation of assembly factors, resulting in a more effective *assembly phase*. Increased numbers of periodic patches could ensure improved stabilization of the young axon, as deletion of spectrin leads to breakage of axons in worms (Hammarlund et al. 2007). The transient nature of the early increase in periodicity could be linked to the improved outgrowth speed at later time points after axotomy. Increased periodicity could, therefore, be hindering to increased axonal outgrowth speed. A different explanation for the decrease of periodicity could be the increased outgrowth speed itself, as increased outgrowth speed and unchanged speed of MPS formation would result in lower percentages of spectrin periodicity.

On the one hand, the findings of this study show that a completely developed MPS is not necessary for axonal regeneration, as regenerating axons do not have the same level of periodicity as a mature, non-axotomized axon has in the more proximal parts of its axon. On the other hand, it is remarkable that a developing MPS is indeed present in regenerating axons, in fact, at an even higher degree, and at a very early time point. This suggests that early re-formation of the MPS is essential for early regeneration, possibly caused by a more effective *assembly phase*.

4.7 Calpeptin increases spectrin periodicity

The increase in spectrin periodicity upon treatment of axons with calpeptin suggests that inhibition of calpain using calpeptin increases MPS formation to some degree. Whether this happens during degeneration, regeneration, or both remains unclear. This finding stands in contrast to previous work, where the incubation of aplysia neurons with calpeptin prevented the formation of a GC (Gitler and Spira 2002). In the current experimental model, axons were incubated with calpeptin for 1 h before the axotomy. The axotomy itself was performed using media not containing calpeptin. Due to the short duration of axotomy (1 – 5 min), it was assumed that calpeptin levels were still sufficient to inhibit calpain activity and to cause the increase of spectrin periodicity. Therefore, a possible explanation for these contradicting results could be the different cell types and species used. The role of calpain in the formation of a GC after axotomy in aplysia neurons is studied well, while it is still widely unknown in vertebrate neurons. Still, the results obtained in this study identify calpeptin as a promising research drug for affecting the MPS in regenerating and degenerating axons.

The effect of calpeptin on an increased MPS formation seems to be tied to the increased length of periodic patches, possibly influencing the *elongation phase*. This is especially interesting, as the transient increase of periodicity in untreated regenerating axons was caused by an increased number of periodic patches. Thus, it can be suggested that this difference is caused by two distinct mechanisms.

4.8 Calpain inhibition leads to enhanced axonal regeneration

To further understand the role of the MPS in axonal regeneration, it is interesting to understand whether the presence of MPS benefits axonal regeneration or limits it. This study suggests that enhancing the MPS formation using calpeptin leads to enhanced axonal regeneration, as more axons regenerate in calpeptin-treated chambers. The length of the regenerating axonal segment, however, was not changed upon treatment. Further research needs to be conducted to explore the exact mechanism of this effect, and possible clinical applications of MPS formation enhancement in trauma or degenerative diseases should be investigated.

4.9 Limitations

Like any study, this study has a few limitations. The time-consuming semi-manual nanoscale evaluation of periodicity parameters comes at the cost of a limited sample size. This could be enhanced by employing unbiased automated sampling and quantitative analysis, as shown before (Barabas et al. 2017; Unsain et al. 2018). Unfortunately, this was not possible in the current specific analysis. Furthermore, the timeframe needed for a regenerating axon to establish a completely mature MPS is still unknown. As a mature MPS was not seen up to 6 h after axotomy, later time points should be evaluated, or axons should be followed further back at the 24-hour time point. Also, in this study, dynamic implications were drawn from fixed cells, so caution is advised when interpreting these findings. Therefore, live-STED imaging could improve the understanding of MPS formation, both in regenerating and in non-axotomized outgrowing axons. Another limiting factor is the use of embryonic cortical neurons, which have different capabilities for regeneration compared to mature cortical neurons. Also, the use of a monoculture of cortical neurons does not represent the complex cellular structures of a brain, as glial cells, extracellular matrix, and a plethora of different other factors are absent. While calpeptin is a good inhibitor of calpain, the enzyme calpain itself has pleiotropic effects, which cannot be reduced to its effect on spectrin during axotomy.

Despite these limitations, the current study can certainly improve our understanding of the development and maturation of the MPS in outgrowing and regenerating axons.

4.10 Conclusion and implications

This study aimed to characterize the development and formation of the MPS in non-axotomized outgrowing and in regenerating axons and to evaluate the effect of calpain inhibition on the regeneration of neurons.

STED microscopy revealed that growing axons exhibit a distinct spatial and temporal increase of spectrin periodicity. This increase happens in a gradient from the distal growth cone towards the soma. The identification of periodic patches, made up of periodically distributed spectrin tetramers, as the building blocks of the MPS, provides new insight into the formation of the MPS. This study proposes a sequence of MPS formation in three phases. In the *assembly phase*, periodic patches are seeded close to the GC. As the axon elongates, the number of patches doubles and the patches extend in length, the *elongation phase*. Finally, the periodic patches coalesce and form the mature MPS during the *coalescence phase*. The MPS develops faster and in more distal locations in regenerating axons than in non-axotomized axons, however this was a transient effect. The calpain inhibitor calpeptin was identified as a promising drug for enhancing MPS formation, and treatment resulted in a higher number of regenerating axons.

The results obtained in the current study raise further questions. What molecular mechanisms are in play to facilitate the assembly and elongation of periodic patches? Is the GC or its neck the site of periodic patch assembly? Furthermore, the development of the MPS in periodic patches was investigated in only one neuronal type in one species. It seems likely that this is a universal principle, but more neuronal cell types and species need to be evaluated. Using automated unbiased sampling and quantitative analysis, a high throughput of axons of different cell types could be analyzed. Calpeptin and other reagents capable of affecting the MPS should be considered for further research on molecular mechanisms of the MPS.

5 Abstract

The cytoskeleton is essential for axon outgrowth and regeneration. It must be able to tolerate mechanical force and torsion while also allowing for adaptation and response to trauma or injury, such as axonal lesions. Recent breakthroughs in super-resolution imaging have revealed that the cytoskeletal proteins actin, spectrin, and adducin form highly periodic structures in the axon called the membrane-associated periodic skeleton (MPS). Little is known about the exact sequence of MPS formation and development in physiologically outgrowing axons, nor in regenerating axons.

Using stimulated emission depletion microscopy, this study provides an extensive nanoscale examination of MPS formation in growing axons of primary cortical rat neurons in microfluidic chambers and the cytoskeletal alterations that occur following axotomy.

This study shows that outgrowing axons exhibit an increase in spectrin periodicity in a gradient from the distal growth cone towards the soma. It is further demonstrated here that periodic arrangements of βII-spectrin (periodic patches) serve as the building blocks in MPS formation. These periodic patches grow in size and number and eventually coalesce to form the mature MPS. In contrast to physiologically outgrowing axons, the MPS transiently develops more quickly and at more distal regions in regenerating axons. The inhibition of calpain, a spectrin-cleaving enzyme, using calpeptin leads to enhanced periodicity and more regenerating axons.

6 Appendix

6.1 Macro code: Segmenter

This macro can be used for the segmentation of nonlinear structures (axons) into segments with a defined length. The pixel data itself is not altered, as an overlay is created. The segments are enumerated with the distance from the start of the segmentation line (GC). The defined length for a segment in this code is 10 µm.

```
macro "Segmenter" {
        /*
         * written by Max Hofmann and Kevin Schmidt
         */
macro "tick marks Tool - C00cT0f16T" {
   if (roiManager('count')<1) exit("Add at least one ROI to the ROI Manager.");
   Dialog.create("Segmenter");
   if (roiManager("index")==-1) exit("Please select one ROI from the ROI
manager.");
   Dialog.addMessage("The overlay will be generated for the currently selected
ROI.");
   Dialog.show();
   ROI=roiManager("index");
   roiManager('select', ROI);
run("Interpolate", "interval=1 adjust");
getSelectionCoordinates(xp, yp);
run("Add Selection...", "stroke=green width=0.05");
List.setMeasurements();
total = List.getValue("Length");
interval = 10;
steps = (total/interval);
xm=0;
ym=0;
xt=0;
yt=0;
fx=30;
angle_line=0;
setFont("Sanserif", 20, "Bold");
for (i=0;i<steps;i++) {
   xm=xp[i*xp.length/steps];
   ym=yp[i*xp.length/steps];
   if (i==0) {
      makeLine(xp[i*xp.length/steps], yp[i*xp.length/steps],
xp[(i*xp.length/steps)+50], yp[(i*xp.length/steps)+50]);
   }
   else {
      makeLine(xp[(i*xp.length/steps)-50], yp[(i*xp.length/steps)-50],
xp[(i*xp.length/steps)+50], yp[(i*xp.length/steps)+50]);
   }
   angle_line=getValue("Angle");
   if ((angle_line<=90 && angle_line>=0) || (angle_line<=-90 && angle_line>=-
180)) {
```

```
      fx=30;
   }
   else {
      fx=-60;
   }
   xt=xm+fx;
   yt=ym+30;
   makePoint(xm, ym, "large blue circle");
   run("Add Selection...","");
   makeText(i*10, xt, yt);
   run("Add Selection...","");
}
}
}
```

7 List of references

Abbe E (1873): Beiträge zur Theorie des Mikroskops und der mikroskopischen Wahrnehmung. Arch Mikros Anat 9, 413–468

Apostolova I, Irintchev A, Schachner M (2006): Tenascin-R restricts posttraumatic remodeling of motoneuron innervation and functional recovery after spinal cord injury in adult mice. J Neurosci 26, 7849–7859

Baas PW, Deitch JS, Black MM, Banker GA (1988): Polarity orientation of microtubules in hippocampal neurons: Uniformity in the axon and nonuniformity in the dendrite. Proc Natl Acad Sci U S A 85, 8335–8339

Bär J, Kobler O, van Bommel B, Mikhaylova M (2016): Periodic F-actin structures shape the neck of dendritic spines. Sci Rep 6, 37136

Barabas FM, Masullo LA, Bordenave MD, Giusti SA, Unsain N, Refojo D, Cáceres A, Stefani FD (2017): Automated quantification of protein periodic nanostructures in fluorescence nanoscopy images: Abundance and regularity of neuronal spectrin membrane-associated skeleton. Sci Rep 7, 16029

Bennett V, Davis J, Fowler WE (1982): Brain spectrin, a membrane-associated protein related in structure and function to erythrocyte spectrin. Nature 299, 126–131

Berghs S, Aggujaro D, Dirkx Jr. R, Maksimova E, Stabach P, Hermel J-M, Zhang J-P, Philbrick W, Slepnev V, Ort T, et al. (2000): βiv Spectrin, a New Spectrin Localized at Axon Initial Segments and Nodes of Ranvier in the Central and Peripheral Nervous System. J Cell Biol 151, 985–1002

Blom H, Brismar H (2014): STED microscopy: increased resolution for medical research? J Intern Med 276, 560–578

Bradke F, Fawcett JW, Spira ME (2012): Assembly of a new growth cone after axotomy: The precursor to axon regeneration. Nat Rev Neurosci 13, 183–193

Brown JW, Bullitt E, Sriswasdi S, Harper S, Speicher DW, McKnight CJ (2015): The Physiological Molecular Shape of Spectrin: A Compact Supercoil Resembling a Chinese Finger Trap. PLoS Comput Biol 11, e1004302

Buck KB, Zheng JQ (2002): Growth cone turning induced by direct local modification of microtubule dynamics. J Neurosci 22, 9358–9367

Caccamo DV, Herman MM, Frankfurter A, Katsetos CD, Collins VP, Rubinstein LJ (1989): An immunohistochemical study of neuropeptides and neuronal cytoskeletal proteins in the neuroepithelial component of a spontaneous murine ovarian teratoma. Primitive neuroepithelium displays immunoreactivity for neuropeptides and neuron-associated β-tubul. Am J Pathol 135, 801–813

Costa AR, Sousa MM (2021): The role of the membrane-associated periodic skeleton in axons. Cell Mol Life Sci 78, 5371–5379

Costa AR, Sousa SC, Pinto-Costa R, Mateus JC, Lopes CDF, Costa AC, Rosa D, Machado D, Pajuelo L, Wang X, et al. (2020): The membrane periodic skeleton is an actomyosin network that regulates axonal diameter and conduction. Elife 9, e55471

Cote RH, Borisy GG (1981): Head-to-tail polymerization of microtubules in vitro. J Mol Biol 150, 577–599

D'Este E, Kamin D, Göttfert F, El-Hady A, Hell SW (2015): STED Nanoscopy Reveals the Ubiquity of Subcortical Cytoskeleton Periodicity in Living Neurons. Cell Rep 10, 1246–1251

D'Este E, Kamin D, Velte C, Göttfert F, Simons M, Hell SW (2016): Subcortical cytoskeleton periodicity throughout the nervous system. Sci Rep 6, 22741

Dent EW, Gertler FB (2003): Cytoskeletal Dynamics and Transport in Growth Cone Motility and Axon Guidance. Neuron 40, 209–227

Dubey S, Bhembre N, Bodas S, Veer S, Ghose A, Callan-Jones A, Pullarkat P, Sens P (2020): The axonal actin-spectrin lattice acts as a tension buffering shock absorber. Elife 9, e51772

Fan A, Tofangchi A, Kandel M, Popescu G, Saif T (2017): Coupled circumferential and axial tension driven by actin and myosin influences in vivo axon diameter. Sci Rep 7, 14188

Fishman HM, Bittner GD (2003): Vesicle-mediated restoration of a plasmalemmal barrier in severed axons. News Physiol Sci 18, 115–118

Fitch MT, Silver J (2008): CNS injury, glial scars, and inflammation: Inhibitory extracellular matrices and regeneration failure. Exp Neurol 209, 294–301

Flynn KC, Hellal F, Neukirchen D, Jacob S, Tahirovic S, Dupraz S, Stern S, Garvalov BK, Gurniak C, Shaw AE, et al. (2012): ADF/cofilin-mediated actin retrograde flow directs neurite formation in the developing brain. Neuron 76, 1091–1107

Fowler VM (2013): The human erythrocyte plasma membrane: a Rosetta Stone for decoding membrane-cytoskeleton structure. Curr Top Membr 72, 39–88

Friede RL, Samorajski T (1970): Axon caliber related to neurofilaments and microtubules in sciatic nerve fibers of rats and mice. Anat Rec 167, 379–387

Galiano MR, Jha S, Ho TSY, Zhang C, Ogawa Y, Chang KJ, Stankewich MC, Mohler PJ, Rasband MN (2012): A distal axonal cytoskeleton forms an intra-axonal boundary that controls axon initial segment assembly. Cell 149, 1125–1139

Gardner WJ, McCubbin JW (1956): Auriculotemporal syndrome; gustatory sweating due to misdirection of regenerated nerve fibers. J Am Med Assoc 160, 272–277

Ghisleni A, Galli C, Monzo P, Ascione F, Fardin MA, Scita G, Li Q, Maiuri P, Gauthier NC (2020): Complementary mesoscale dynamics of spectrin and acto-myosin shape membrane territories during mechanoresponse. Nat Commun 11, 5108

Gitler D, Spira ME (2002): Short window of opportunity for calpain induced growth cone formation after axotomy of Aplysia neurons. J Neurobiol 52, 267–279

Graf von Keyserlingk D, Schramm U (1984): Diameter of axons and thickness of myelin sheaths of the pyramidal tract fibres in the adult human medullary pyramid. Anat Anz 157, 97–111

Greenberg MM, Leitao C, Trogadis J, Stevens JK (1990): Irregular geometries in normal unmyelinated axons: A 3D serial EM analysis. J Neurocytol 19, 978–988

Grum VL, Li D, MacDonald RI, Mondragón A (1999): Structures of two repeats of spectrin suggest models of flexibility. Cell 98, 523–535

Hammarlund M, Jorgensen EM, Bastiani MJ (2007): Axons break in animals lacking β-spectrin. J Cell Biol 176, 269–275

Han B, Zhou R, Xia C, Zhuang X (2017): Structural organization of the actin-spectrin–based membrane skeleton in dendrites and soma of neurons. Proc Natl Acad Sci U S A 114, E6678–E6685

Hauser M, Yan R, Li W, Repina NA, Schaffer DV, Xu K (2018): The Spectrin-Actin-Based Periodic Cytoskeleton as a Conserved Nanoscale Scaffold and Ruler of the Neural Stem Cell Lineage. Cell Rep 24, 1512–1522

He J, Zhou R, Wu Z, Carrasco MA, Kurshan PT, Farley JE, Simon DJ, Wang G, Han B, Hao J, et al. (2016): Prevalent presence of periodic actin-spectrin-based membrane skeleton in a broad range of neuronal cell types and animal species. Proc Natl Acad Sci U S A 113, 6029–6034

Heidemann SR, Lamoureux P, Buxbaum RE (1990): Growth cone behavior and production of traction force. J Cell Biol 111, 1949–1957

Hell SW, Wichmann J (1994): Breaking the diffraction resolution limit by stimulated emission: stimulated-emission-depletion fluorescence microscopy. Opt Lett 19, 780–782

Hofmann M, Biller L, Michel U, Bähr M, Koch JC (2021): Cytoskeletal assembly in axonal outgrowth

and regeneration analyzed on the nanoscale. bioRxiv 2021.11.04.467310

Hofmann M, Biller L, Michel U, Bähr M, Koch JC (2022): Cytoskeletal assembly in axonal outgrowth and regeneration analyzed on the nanoscale. Sci Rep 12, 14387

Holleran EA, Tokito MK, Karki S, Holzbaur ELF (1996): Centractin (ARP1) associates with spectrin revealing a potential mechanism to link dynactin to intracellular organelles. J Cell Biol 135, 1815–1829

Houschyar KS, Momeni A, Pyles MN, Cha JY, Maan ZN, Duscher D, Jew OS, Siemers F, van Schoonhoven J (2016): The Role of Current Techniques and Concepts in Peripheral Nerve Repair. Plast Surg Int 2016, 4175293

Huebner EA, Strittmatter SM (2009): Axon regeneration in the peripheral and central nervous systems. Results Probl Cell Differ 48, 339–351

Ikeda Y, Dick KA, Weatherspoon MR, Gincel D, Armbrust KR, Dalton JC, Stevanin G, Dürr A, Zühlke C, Bürk K, et al. (2006): Spectrin mutations cause spinocerebellar ataxia type 5. Nat Genet 38, 184–190

Kapitein LC, Hoogenraad CC (2011): Which way to go? Cytoskeletal organization and polarized transport in neurons. Mol Cell Neurosci 46, 9–20

Kevenaar JT, Hoogenraad CC (2015): The axonal cytoskeleton: from organization to function. Front Mol Neurosci 8, 44

Koch JC, Barski E, Lingor P, Bähr M, Michel U (2011): Plasmids containing NRSE/RE1 sites enhance neurite outgrowth of retinal ganglion cells via sequestration of REST independent of NRSE dsRNA expression. FEBS J 278, 3472–3483

Kovesi P (2015): Good Colour Maps: How to Design Them. arXiv[csGR] 1509.03700

Ledbetter MC, Porter KR (1963): A "microtubule" in plant cell fine structure. J Cell Biol 19, 239–250

Leite SC, Sousa MM (2016): The neuronal and actin commitment: Why do neurons need rings? Cytoskeleton 73, 424–434

Leite SC, Sampaio P, Sousa VF, Nogueira-Rodrigues J, Pinto-Costa R, Peters LL, Brites P, Sousa MM (2016): The Actin-Binding Protein α-Adducin Is Required for Maintaining Axon Diameter. Cell Rep 15, 490–498

Leterrier C, Dubey P, Roy S (2017): The nano-architecture of the axonal cytoskeleton. Nat Rev Neurosci 18, 713–726

Levine J, Willard M (1981): Fodrin: axonally transported polypeptides associated with the internal periphery of many cells. J Cell Biol 90, 631–642

Li H, Yang J, Tian C, Diao M, Wang Q, Zhao S, Li S, Tan F, Hua T, Qin Y, et al. (2020): Organized cannabinoid receptor distribution in neurons revealed by super-resolution fluorescence imaging. Nat Commun 11, 5699

Liu CH, Rasband MN (2019): Axonal spectrins: Nanoscale organization, functional domains and spectrinopathies. Front Cell Neurosci 13, 234

Liu CN, Chambers WW (1958): Intraspinal Sprouting of Dorsal Root Axons: Development of New Collaterals and Preterminals Following Partial Denervation of the Spinal Cord in the Cat. Arch Neurol Psychiatry 79, 46–61

Lorenzo DN (2020): Cargo hold and delivery: Ankyrins, spectrins, and their functional patterning of neurons. Cytoskeleton 77, 129–148

Lorenzo DN, Badea A, Zhou R, Mohler PJ, Zhuang X, Bennett V (2019): βII-spectrin promotes mouse brain connectivity through stabilizing axonal plasma membranes and enabling axonal organelle transport. Proc Natl Acad Sci U S A 116, 15686–15695

Lowery LA, Van Vactor D (2009): The trip of the tip: Understanding the growth cone machinery.

Nat Rev Mol Cell Biol 10, 332–343

Lu W, Fox P, Lakonishok M, Davidson MW, Gelfand VI (2013): Initial neurite outgrowth in Drosophila neurons is driven by kinesin-powered microtubule sliding. Curr Biol 23, 1018–1023

Lukinavičius G, Reymond L, D'Este E, Masharina A, Göttfert F, Ta H, Güther A, Fournier M, Rizzo S, Waldmann H, et al. (2014): Fluorogenic probes for live-cell imaging of the cytoskeleton. Nat Methods 11, 731–733

Lux IV SE (2016): Anatomy of the red cell membrane skeleton: unanswered questions. Blood 127, 187–199

Marchesi VT, Steers EJ (1968): Selective solubilization of a protein component of the red cell membrane. Science 159, 203–204

Matsuoka Y, Li X, Bennett V (2000): Adducin: Structure, function and regulation. Cell Mol Life Sci 57, 884–895

Mitchison T, Kirschner M (1984): Dynamic instability of microtubule growth. Nature 312, 237–242

Mitchison TJ (1993): Localization of an exchangeable GTP binding site at the plus end of microtubules. Science 261, 1044–1047

Morris RL, Hollenbeck PJ (1995): Axonal transport of mitochondria along microtubules and F-actin in living vertebrate neurons. J Cell Biol 131, 1315–1326

Parker F, Baboolal TG, Peckham M (2020): Actin mutations and their role in disease. Int J Mol Sci 21, 3371

Pasterkamp RJ, Anderson PN, Verhaagen J (2001): Peripheral nerve injury fails to induce growth of lesioned ascending dorsal column axons into spinal cord scar tissue expressing the axon repellent Semaphorin3A. Eur J Neurosci 13, 457–471

Pollard TD, Cooper JA (2009): Actin, a central player in cell shape and movement. Science 326, 1208–1212

Ramon y Cajal S (1890): Notas anatómicas I. Sobre la aparición de las expansiones celulares en la médula embrionaria. Gac Med Cataluña 12, 413–419

Sahly I, Khoutorsky A, Erez H, Prager-Khoutorsky M, Spira ME (2006): On-line confocal imaging of the events leading to structural dedifferentiation of an axonal segment into a growth cone after axotomy. J Comp Neurol 494, 705–720

Sahu MP, Nikkilä O, Lågas S, Kolehmainen S, Castrén E (2019): Culturing primary neurons from rat hippocampus and cortex. Neuronal Signal 3, NS20180207

Schaefer AW, Kabir N, Forscher P (2002): Filopodia and actin arcs guide the assembly and transport of two populations of microtubules with unique dynamic parameters in neuronal growth cones. J Cell Biol 158, 139–152

Schindelin J, Arganda-Carreras I, Frise E, Kaynig V, Longair M, Pietzsch T, Preibisch S, Rueden C, Saalfeld S, Schmid B, et al. (2012): Fiji: an open-source platform for biological-image analysis. Nat Methods 9, 676–682

Sengottuvel V, Leibinger M, Pfreimer M, Andreadaki A, Fischer D (2011): Taxol facilitates axon regeneration in the mature CNS. J Neurosci 31, 2688–2699

Takeda S, Yamazaki H, Seog DH, Kanai Y, Terada S, Hirokawa N (2000): Kinesin superfamily protein 3 (KIF3) motor transports fodrin-associating vesicles important for neurite building. J Cell Biol 148, 1255–1265

Taylor AM, Blurton-Jones M, Rhee SW, Cribbs DH, Cotman CW, Jeon NL (2005): A microfluidic culture platform for CNS axonal injury, regeneration and transport. Nat Methods 2, 599–605

Taylor L, Jones L, Tuszynski MH, Blesch A (2006): Neurotrophin-3 gradients established by lentiviral gene delivery promote short-distance axonal bridging beyond cellular grafts in the injured spinal cord. J Neurosci 26, 9713–9721

Tedeschi A, Bradke F (2017): Spatial and temporal arrangement of neuronal intrinsic and extrinsic mechanisms controlling axon regeneration. Curr Opin Neurobiol 42, 118–127

Tessier-Lavigne M, Goodman CS (1996): The molecular biology of axon guidance. Science 274, 1123–1133

Thévenaz P, Unser M (2007): User-friendly semiautomated assembly of accurate image mosaics in microscopy. Microsc Res Tech 70, 135–146

Tian N, Leshchyns'ka I, Welch JH, Diakowski W, Yang H, Schachner M, Sytnyk V (2012): Lipid raft-dependent endocytosis of close homolog of adhesion molecule L1 (CHL1) promotes neuritogenesis. J Biol Chem 287, 44447–44463

Unsain N, Bordenave MD, Martinez GF, Jalil S, Von Bilderling C, Barabas FM, Masullo LA, Johnstone AD, Barker PA, Bisbal M, et al. (2018): Remodeling of the Actin/Spectrin Membrane-associated Periodic Skeleton, Growth Cone Collapse and F-Actin Decrease during Axonal Degeneration. Sci Rep 8, 3007

Vassilopoulos S, Gibaud S, Jimenez A, Caillol G, Leterrier C (2019): Ultrastructure of the axonal periodic scaffold reveals a braid-like organization of actin rings. Nat Commun 10, 5803

Wang G, Simon DJ, Wu Z, Belsky DM, Heller E, O'Rourke MK, Hertz NT, Molina H, Zhong G, Tessier-Lavigne M, et al. (2019): Structural plasticity of actin-spectrin membrane skeleton and functional role of actin and spectrin in axon degeneration. Elife 8, e38730

Wang T, Li W, Martin S, Papadopulos A, Joensuu M, Liu C, Jiang A, Shamsollahi G, Amor R, Lanoue V, et al. (2020): Radial contractility of actomyosin rings facilitates axonal trafficking and structural stability. J Cell Biol 219, e201902001

Weisenberg RC (1972): Microtubule formation in vitro in solutions containing low calcium concentrations. Science 177, 1104–1105

Xu K, Zhong G, Zhuang X (2013): Actin, spectrin, and associated proteins form a periodic cytoskeletal structure in axons. Science 339, 452–456

Zhang JN, Michel U, Lenz C, Friedel CC, Köster S, D'Hedouville Z, Tönges L, Urlaub H, Bähr M, Lingor P, et al. (2016): Calpain-mediated cleavage of collapsin response mediator protein-2 drives acute axonal degeneration. Sci Rep 6, 37050

Zhang Y, Abiraman K, Li H, Pierce DM, Tzingounis AV, Lykotrafitis G (2017): Modeling of the axon membrane skeleton structure and implications for its mechanical properties. PLoS Comput Biol 13, e1005407

Zhong G, He J, Zhou R, Lorenzo D, Babcock HP, Bennett V, Zhuang X (2014): Developmental mechanism of the periodic membrane skeleton in axons. Elife 3, e04581

Zhou R, Han B, Xia C, Zhuang X (2019): Membrane-associated periodic skeleton is a signaling platform for RTK transactivation in neurons. Science 365, 929–934

Zhou R, Han B, Nowak R, Lu Y, Heller E, Xia C, Chishti AH, Fowler VM, Zhuang X (2022): Proteomic and functional analyses of the periodic membrane skeleton in neurons. Nat Commun 13, 3196

Zolotukhin S, Byrne BJ, Mason E, Zolotukhin I, Potter M, Chesnut K, Summerford C, Samulski RJ, Muzyczka N (1999): Recombinant adeno-associated virus purification using novel methods improves infectious titer and yield. Gene Ther 6, 973–985

Danksagung

Bedanken möchte ich mich zuerst bei meinem Doktorvater, Herrn **PD Dr. med. Jan C. Koch** für seine große Unterstützung, seine Begeisterung und seinen Optimismus und für das sehr große Vertrauen, das er mir entgegengebracht hat. Dank ihm durfte ich einen großen Gestaltungsfreiraum bei der Ausrichtung der Experimente im Labor genießen und verschiedene Nebenexperimente durchführen, sowie die Betreuung zweier Laborrotationen von Masterstudenten realisieren. Ich danke ihm außerdem für zügige und ausführliche Korrekturen, seine Verfügbarkeit und sein offenes Ohr für meine Fragen.

Ein großer Dank gilt auch Frau **Elisabeth Barski**, die mich tatkräftig bei der Arbeit im Labor unterstützte. Ihr großes Wissen und ihr Interesse, alle möglichen Experimente zu realisieren, haben einen großen Teil zu dieser Dissertation beigetragen. Ihre akribische Arbeitsweise bereicherte die Qualität der in dieser Dissertation durchgeführten Experimente sehr.

Dank gilt auch meinem Zweitbetreuer Herrn **Prof. Dr. rer. nat. Thomas Dresbach** für sein stets konstruktives Feedback. Herrn **Prof. Dr. med. Matthias Bär** danke ich für die Möglichkeit, in seiner Klinik zur promovieren sowie im Bär-Lab-Meeting meine Arbeit vorstellen zu dürfen.

Danke an Herrn **Prof. Dr. Dr. h. c. mult. Stefan W. Hell** für die Möglichkeit, das STED-Mikroskop seiner Arbeitsgruppe zu nutzen. Ebenfalls bedanken möchte ich mich bei **Dr. Stefan Stoldt** für den exzellenten technischen Support bei der Benutzung des STED-Mikroskops. Herrn **Prof. Dr. Uwe Michel** danke ich für die Bereitstellung des Virus zur Transduktion.

Dank gilt auch dem **Vorsprung-Promotionskolleg** für die gewährte Unterstützung, die Seminare, den Vorsprung-Retreat und die Möglichkeit, meine Arbeit bei der Forschungskonferenz der Klinik für Neurologie vorzustellen.